Monthly Notices of the ROYAL ASTRONOMICAL SOCIETY

MNRAS **508,** 453–474 (2021) https://doi.org/10.1093/mnras/stab2517
Advance Access publication 2021 September 9

Global 3D radiation hydrodynamic simulations of proto-Jupiter's convective envelope

Zhaohuan Zhu [1]★ Yan-Fei Jiang,[2] Hans Baehr [1] Andrew N. Youdin,[3] Philip J. Armitage[2,4] and Rebecca G. Martin [1]

[1]*Department of Physics and Astronomy, University of Nevada, Las Vegas, 4505 S. Maryland Parkway, Las Vegas NV 89154-4002, USA*
[2]*Center for Computational Astrophysics, Flatiron Institute, 162 Fifth Avenue, New York NY 10010, USA*
[3]*Steward Observatory & Department of Astronomy, University of Arizona, 933 N Cherry Ave, Tucson AZ 85721, USA*
[4]*Department of Physics and Astronomy, Stony Brook University, Stony Brook, New York NY 11794-3800, USA*

Accepted 2021 August 17. Received 2021 August 12; in original form 2021 June 18

ABSTRACT

The core accretion model of giant planet formation has been challenged by the discovery of recycling flows between the planetary envelope and the disc that can slow or stall envelope accretion. We carry out 3D radiation hydrodynamic simulations with an updated opacity compilation to model the proto-Jupiter's envelope. To isolate the 3D effects of convection and recycling, we simulate both isolated spherical envelopes and envelopes embedded in discs. The envelopes are heated at given rates to achieve steady states, enabling comparisons with 1D models. We vary envelope properties to obtain both radiative and convective solutions. Using a passive scalar, we observe significant mass recycling on the orbital time-scale. For a radiative envelope, recycling can only penetrate from the disc surface until ∼0.1–0.2 planetary Hill radii, while for a convective envelope, the convective motion can 'dredge up' the deeper part of the envelope so that the entire convective envelope is recycled efficiently. This recycling, however, has only limited effects on the envelopes' thermal structure. The radiative envelope embedded in the disc has identical structure as the isolated envelope. The convective envelope has a slightly higher density when it is embedded in the disc. We introduce a modified 1D approach which can fully reproduce our 3D simulations. With our updated opacity and 1D model, we recompute Jupiter's envelope accretion with a 10 $M_\oplus$ core, and the time-scale to runaway accretion is shorter than the disc lifetime as in prior studies. Finally, we discuss the implications of the efficient recycling on the observed chemical abundances of the planetary atmosphere (especially for super-Earths and mini-Neptunes).

Key words: convection – opacity – radiation: dynamics – planets and satellites: formation – planets and satellites: gaseous planets – protoplanetary discs.

1 INTRODUCTION

The core accretion mechanism is one of the leading giant planet formation mechanisms (Perri & Cameron 1974; Mizuno, Nakazawa & Hayashi 1978). It was developed using a combination of static 1D models and quasi-static evolutionary models. In the static models, the planet's envelope structure is calculated for a given core mass given some assumptions on the envelope's thermal structure (Perri & Cameron 1974; Mizuno et al. 1978; Mizuno 1980). Assuming a luminosity that is released by a constant rate of planetesimal accretion (Mizuno 1980), such static solutions suggest a maximum core mass for any given opacity. This maximum core mass is the 'critical core mass', beyond which the envelope is subject to collapse. Although the critical core mass can range widely depending on the given luminosity and disc parameters (Rafikov 2006), it is estimated to be around 10 $M_\oplus$ for Jupiter formation in the Solar Nebula (Mizuno 1980; Stevenson 1982). In assuming that all the luminosity comes from planetesimal accretion, static models ignore energy release from the envelope's Kelvin–Helmholtz (KH) contraction. Thus, these models implicitly assume that the envelope settles on a time-scale much shorter than the core building time-scale or the disc lifetime. We can think of the static models as taking snapshots during the envelope accretion. To properly take into account the envelope's KH contraction, quasi-static evolutionary models have been developed. These models connect different snapshots using energy conservation (Bodenheimer & Pollack 1986; Pollack et al. 1996; Movshovitz et al. 2010). These quasi-static models suggest that Jupiter's formation has three stages: the core building stage, the atmosphere accretion stage, and the run-away stage when the core mass is comparable to the envelope mass. Run-away accretion ends when the planets manage to induce gaseous gaps in protoplanetary discs (Bryden et al. 1999; Alibert et al. 2005; Rosenthal et al. 2020). The quasi-static approach has been extended to model the formation of giant planets in exoplanetary systems (e.g. Lee, Chiang & Ormel 2014; Piso & Youdin 2014; Lee & Chiang 2015; Piso, Youdin & Murray-Clay 2015; Ali-Dib, Cumming & Lin 2020; Chen et al. 2020).

The adequacy of any 1D description of giant planet formation can reasonably be questioned. In addition to convection (as shown in 3D simulations of Ayliffe & Bate 2012) – which can be modelled in 1D but only approximately – 3D numerical simulations show that the flow pattern around embedded planets is highly complex.

★ E-mail: zhaohuan.zhu@unlv.edu

Gas in the disc flows to the planet from the pole, and then leaves the planet from the mid-plane (Machida et al. 2008; Tanigawa, Ohtsuki & Machida 2012). Isothermal (Bate et al. 2003; Fung, Artymowicz & Wu 2015; Ormel, Shi & Kuiper 2015; Béthune & Rafikov 2019), isentropic (Fung et al. 2017), adiabatic (Fung, Zhu & Chiang 2019), and radiation (Paardekooper & Mellema 2008; Ayliffe & Bate 2009; D'Angelo & Bodenheimer 2013; Szulágyi et al. 2016; Cimerman, Kuiper & Ormel 2017; Lambrechts & Lega 2017; Szulágyi & Mordasini 2017) hydrodynamic models all show complicated 3D flow patterns, but the details of the flow patterns are dramatically different among these simulations. In part, the differences arise due to different adopted equations of state (EOS; Fung et al. 2019). Isothermal simulations show a rotationally supported circumplanetary disc (Tanigawa et al. 2012; Wang et al. 2014; Fung et al. 2019), while adiabatic and radiative simulations show a pressure supported sphere. The effect of these 3D flow patterns on giant planet atmosphere accretion is still unclear. Some works suggest that significant 'atmosphere mass recycling' (Ormel et al. 2015) extends all the way to the planetary core or the simulated inner boundary (Cimerman et al. 2017; Béthune & Rafikov 2019). This recycling could stall atmosphere accretion, preventing the planet's run-away accretion (Moldenhauer et al. 2021). Other works suggest that the bound inner envelope is not affected strongly by recycling (Lambrechts & Lega 2017; Fung et al. 2019).

The 1D and 3D approaches have quite different assumptions and produce different results. Both approaches have shortcomings. Although 3D simulations are needed to capture recycling flows, they suffer from limited spatial resolution and a limited time span. It is impractical to simulate Jupiter all the way from the core to the 5 au scale over the 1 Myr KH contraction time-scale. Thus, 3D simulations normally place the inner boundary condition at radii larger than the physical radius of the core (Béthune & Rafikov 2019), and often reduce the opacity by several orders of magnitude to shorten the KH time-scale (Cimerman et al. 2017; Moldenhauer et al. 2021). A promising approach is to combine 3D simulations with 1D models. We can study detailed physical processes and measure key quantities from 3D simulations, and then use these 3D simulations to construct 1D models to study the long-term planet evolution.

Here, we present the results of new 3D simulations of the forming Jupiter's convective envelope. The simulations use an updated opacity, appropriate for both disc and envelope physical conditions, and a radiative transfer scheme that directly solves the time-dependent transfer equation for the specific intensity (Jiang, Stone & Davis 2014). This approach is more accurate than flux-limited diffusion at low and intermediate optical depths. In order to systematically isolate 3D effects due to convection and recycling, and to compare 1D and 3D results, our simulation setup is distinct from prior work in two ways. First, we inject specified luminosities throughout the envelopes so that the envelopes can reach steady states. The steady-state outcome is similar to the traditional static 1D approach, making comparison between 1D models and 3D simulations easier. Secondly, we run 3D simulations of isolated spherical envelopes as well as envelopes that are embedded with the disc. The isolated 3D simulations have identical setups as 1D models, except that convection is simulated self-consistently. By comparing these 3D simulations with 1D radiation-only simulations, we are able to study the effects of convection on the envelope structure. At the same time, the 3D isolated envelope simulations are also similar to the 3D envelopes that are embedded in discs, except for the absence of disc recycling. A comparison between these two types of simulation can therefore quantify the effects of recycling.

The plan of the paper is as follows. We introduce our updated opacity in Section 2 before presenting the simulation methods in Section 3. We present our results in Section 4. After some discussion in Section 5, we conclude in Section 6. We defer some numerical details to the Appendices.

2 OPACITY

Opacity determines the envelope's cooling ability and thus directly controls the envelope's KH contraction and later run-away accretion. Although we know little empirically about the opacity in the planetary envelope itself (which will be affected by pebble accretion and coagulation processes; Podolak 2003; Brouwers & Ormel 2020), the outer envelope is directly connected with the protoplanetary disc, and we have constraints on the disc's dust opacity from ALMA observations. For the deeper parts of the envelope where molecular and atomic opacities dominate, several widely used opacities (e.g. the opacities adopted in the MESA code; Paxton et al. 2011) are not suitable for the conditions of the forming planet's envelope. Thus, we update and generate a new opacity table including dust, molecular, and atomic opacities, spanning a large density and temperature range for our envelope simulations. The Rosseland and Planck mean opacity table can be downloaded at the Github repository.[1]

2.1 Dust opacity

We calculate the dust opacity following Birnstiel et al. (2018). They compared several widely used dust opacities, and calculated a new set of opacities which have been successfully used in the ALMA large program DSHARP (Andrews et al. 2018). The dust is composed of four different materials: water ice (Warren & Brandt 2008), astronomical silicates (Draine 2003), troilite, and refractory organics (Henning & Stognienko 1996). The mass fractions of water ice, silicates, troilite, and refractory organics are 0.2, 0.3291, 0.0743, 0.3966, respectively (Birnstiel et al. 2018). These fractions are not derived from chemical equilibrium calculations. Instead, they are determined based on protoplanetary disc spectral energy distribution (SED) constraints (e.g. the adoption of the low water abundance). Thus, the elemental abundance of the dust component is different from the solar abundance that is used for the molecular and atomic opacity calculations in the following sections. Although chemical equilibrium calculations for the dust components can remedy this inconsistency (Ferguson et al. 2005), we decide to use the dust components that are more consistent with protoplanetary disc observations. We adopt the nominal $q = 3.5$ power-law dust size distribution with a minimum particle size of 10^{-5} cm. We have calculated the opacity for different maximum particle sizes: $a_{\rm max} = 10$ μm, 1 mm, 1 cm, and 10 cm. The details of the opacity calculation can be found in Birnstiel et al. (2018).[2]

With increasing temperature, the four materials considered sublimate one after another. We adopt the dust sublimation temperatures in table 3 of Pollack et al. (1994) to decide which material to remove at different temperatures. The sublimation temperatures of the water ice and refractory organics are from 'Water ice in discs' and 'Refractory organics in discs' in Pollack et al. (1994). When the gas density is beyond the density range provided by Pollack et al. (1994), which is between 10^{-18} and 10^{-4} g cm^{-3}, we just use the limiting density

[1] https://github.com/zhuzh1983/combined-opacity
[2] https://github.com/birnstiel/dsharp_opac

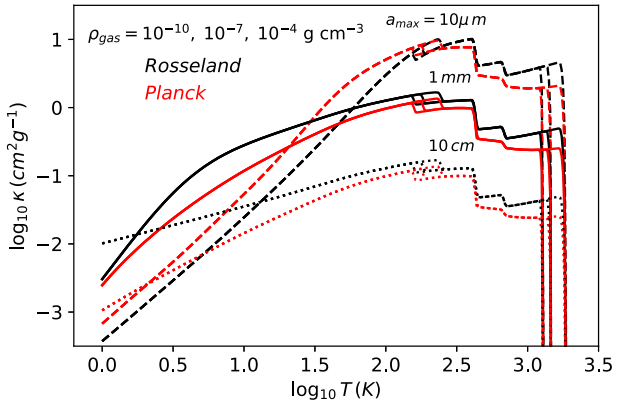

Figure 1. The Rosseland mean (black curves) and Planck mean (red curves) opacities for dust with different maximum particle size, $a_{\max}$ (three different line types: dashed, solid, and dotted curves). To show that the dust sublimation temperature depends on the gas density, there are three different curves (almost overlapping each other) for each type that are calculated under three different gas densities (10^{-10}, 10^{-7}, and 10^{-4} g cm^{-3}).

(10^{-18} or 10^{-4} g cm^{-3}). Since dust gradually sublimates over a temperature range around the sublimation temperature, we smooth out the opacity transition around the dust sublimation temperature ($T_{\rm sub}$) using a sin function,

$$\kappa(T) = \kappa_{lT} + (\kappa_{hT} - \kappa_{lT})\left(1 - \frac{1}{2}\left(\sin\left(\frac{T - T_{\rm sub}}{\Delta T_{\rm sub}}\pi\right) + 1\right)\right), \quad \text{if } T_{\rm sub} - \frac{\Delta T_{\rm sub}}{2} < T < T_{\rm sub} + \frac{\Delta T_{\rm sub}}{2}, \tag{1}$$

where κ_{lT} and κ_{hT} are opacities before and after one particular material is sublimated. To determine the width of the transition temperature ($\Delta T_{\rm sub}$), we use the GRAINS code (Petaev 2009; Li et al. 2020) and fig. 4 in Li et al. (2020) to estimate $\Delta T_{\rm sub} = T_{\rm sub}/10 \times (\log_{10}(P/{\rm bar})/16 + 1)$, where P is the gas pressure. The pressure dependent term accounts for the fact that the transition is smoother in a higher pressure environment.

The Rosseland mean and Planck mean opacities for dust with different $a_{\max}$ are shown in Fig. 1. When the temperature increases, different dust components start to sublimate. The sublimation occurs at a higher temperature in a higher pressure environment, except for troilite and refractory organics whose sublimation temperature was given as a single value in Pollack et al. (1994).

2.2 Molecular opacity

For the gas opacity at low temperature (dominated by the molecular opacity), we adopt the opacity table provided by Freedman et al. (2014).[3] This opacity table covers gaseous pressure from 10^{-6} to 300 bar, and temperature from 75 to 4000 K. The corresponding gaseous density range is from $\sim 10^{-10}$ to 10^{-3} g cm^{-3} (Fig. 2), which is significantly broader than the density or pressure range in previous gaseous opacity tables (e.g. Ferguson et al. 2005; Freedman, Marley & Lodders 2008). On the other hand, deep within the forming planet's envelope, the gaseous density can be much higher, reaching 1 g cm^{-3}. Thus, we use the analytical fit provided in Freedman et al. (2014, equations 3–5) to derive the Rosseland mean opacity for densities higher than $\sim 10^{-3}$ g cm^{-3} and lower than 1 g cm^{-3}. Applying the analytical fit to high densities leads to a smooth transition to atomic opacities in the next section. However, we caution that there is no detailed opacity calculation to show that such an extension of the analytical fit to high density is valid. For Planck mean opacities, the analytical fit formula has not been provided. Thus, we simply assume that the Planck mean opacity at densities beyond the table range in Freedman et al. (2014) is the same as the Planck mean opacity at the highest density in the table at that temperature. For opacity at densities lower than the provided table range, we also assume that the opacity is the same as the opacity at the lowest density in the table.

2.3 Atomic opacity

At higher temperatures where molecules have been dissociated and the atomic opacity dominates, we adopt the Los Alamos National Lab (LANL) new generation opacity table (Colgan et al. 2016).[4] This new LANL opacity table is LANL's recent opacity effort using their ATOMIC opacity and plasma modelling code (Magee et al. 2004; Hakel et al. 2006) with their atomic data (Fontes et al. 2015). It provides opacities for elements from hydrogen through zinc for a wide range of temperatures (0.5 eV up to 100 kev) and densities (spanning at least 12 orders of magnitude). To derive the solar opacity, we use the solar elemental abundances provided by Asplund et al. (2009; photosphere abundance in their table 1). To calculate the opacities at the metal rich or poor environment, we vary the metal (beyond H and He) abundance accordingly. Both Planck mean and Rosseland mean opacities have been generated using the LANL opacity website. Since protoplanetary discs and planet envelopes are cooler and less dense than stars, we only calculate the opacity with temperatures from 0.5 eV to 1 keV ($\sim$5800 K to 10^7 K) and densities from 10^{-14} to 1 g cm^{-3}. The density range where the LANL opacity is valid depends on the temperature and element considered.

One advantage of the LANL opacity table over the widely used opacities (mainly from Iglesias & Rogers 1996; Ferguson et al. 2005) in MESA (Paxton et al. 2011) is that it includes opacities at high densities and low temperatures, the conditions found in the planet envelope or atmosphere. For example, the MESA opacity table has a maximum opacity at $\rho \sim 0.01$ g cm^{-3} and $T \sim 3 \times 10^4$ K (fig. 3 in Paxton et al. 2011). This maximum opacity is artificial since the adopted radiative opacity in MESA is only valid for $\rho \lesssim 0.01$ g cm^{-3} at $T \sim 3 \times 10^4$ K, as shown in Fig. 2. For $\rho \gtrsim 0.01$ g cm^{-3}, it is interpolated to connect to the electron conduction opacity (Cassisi et al. 2007) at much higher densities. Considering plasma screening and electron degeneracy effects (e.g. Pauli blocking; Armstrong et al. 2014), the LANL radiative opacity is valid at much higher densities, covering the high-pressure range that we are interested in (Fig. 2). By comparison, we can see that, for a given temperature, the LANL radiative opacity continues to rise with density even to our upper density limit of $\rho = 1$ g cm^{-3}, which is dramatically different from the MESA opacity.

2.4 Combining opacities

Various opacities from different opacity data bases, together with their valid range, are shown in Fig. 2. The top three panels show the atomic, molecular, and dust opacities we adopt. The bottom two panels show the solar abundance opacities used in MESA (Paxton et al. 2011) and ATLAS9 (Castelli & Kurucz 2003). Since MESA and ATLAS9 are stellar structure codes, their adopted opacities miss the $\rho - T$ condition of the planet interior.

[3] https://www.ucolick.org/~jfortney/models.htm

[4] https://aphysics2.lanl.gov/apps/

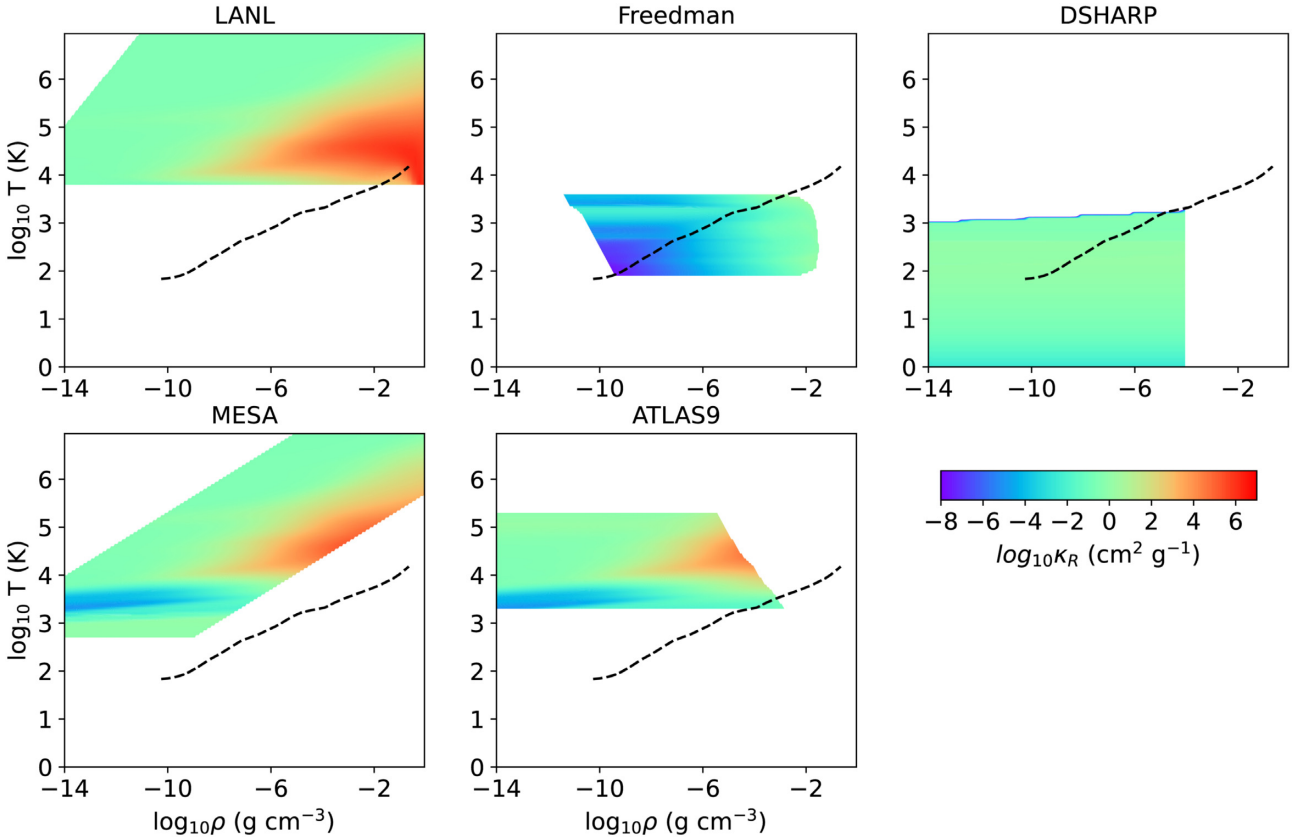

Figure 2. The Rosseland mean opacities at different densities and temperatures from various data bases. The coloured region is where the data are calculated and valid. The dashed curve labels the $\rho - T$ condition of a forming Jupiter's envelope at the cross-over mass, as calculated in Section 5.3.

Our combined opacities (LANL + Freedman + DSHARP) are shown in Fig. 3. At 100 K < T <1000 K, molecules and dust coexist and they all contribute to the total opacity. Since Freedman et al. (2008) didn't provide the monochromatic opacity, we cannot derive the total monochromatic opacity to calculate the mean opacities. Thus, we simply pick the maximum between the molecular and dust mean opacities as the total opacity. Considering that the molecular opacity is normally significantly smaller than the dust opacity, the derived opacity should approximate the real mean opacity reasonably well. For the $\rho - T$ region that does not have valid opacity data, we use the opacity at the smallest or largest available density at that specific temperature, except for the molecular opacity (the detailed interpolation scheme for the molecular opacity is discussed in Section 2.2).

To verify our combined opacities, we compare our mean opacities with the MESA and ATLAS9 opacities in Fig. 4. Our opacities are valid over a much larger $\rho - T$ parameter space. In the common $\rho - T$ parameter space where the different opacity data bases are all valid, our opacities agree with the other opacities quite well. These combined opacities are significant updates to our previously compiled opacities for protoplanetary disc numerical simulations (Zhu, Hartmann & Gammie 2009; Zhu et al. 2012). After deriving this new opacity table, we are ready to use it in our numerical simulations.

3 NUMERICAL METHOD

We solve the hydrodynamical equations using ATHENA++ (Stone et al. 2020). ATHENA++ is the successor of ATHENA that uses a higher order Godunov scheme for magnetohydrodynamic (MHD) and the constrained transport (CT) to conserve the divergence-free property for magnetic fields (Gardiner & Stone 2005, 2008; Stone et al. 2008). The geometric source terms in curvilinear coordinates (e.g. in cylindrical and spherical-polar coordinates) are specifically implemented to conserve angular momentum to machine precision. This property is crucial for disc simulations. In this work, we further extend the angular momentum conservation property to the rotating frame, as detailed in Appendix A.

We have used two different radiation modules to solve the radiative transfer equation and to couple radiation with the fluid equations. Both modules directly solve the time-dependent radiative transfer equation for the specific intensity (Jiang et al. 2014). Unlike the commonly used flux-limited diffusion approximation (Levermore & Pomraning 1981) and the M1 closure method (González, Audit & Huynh 2007; Skinner & Ostriker 2013), solving the specific intensity equation does not suffer the shadowing problem or the ray crossing problem (Davis, Stone & Jiang 2012). We first use the method of Jiang et al. (2014) to explicitly solve the radiative transfer equation. Since the characteristic speed in the transport step is the speed of light, solving this equation explicitly requires very small numerical time-steps. Thus, we adopt the reduced speed of light approach as in Zhang et al. (2018). Although this explicit method is numerically stable and robust, the reduced speed of light could lead to inaccurate light crossing and diffusion time-scales (e.g. Zhang et al. 2018; Zhu, Jiang & Stone 2020). Thus, after the simulation settles to a steady state (five planetary orbits for 3D simulations), we restart the simulations using the implicit method of Jiang (2021). Although the implicit method is slow due to the iteration steps and the speed of light is still reduced in some cases to speed up the convergence, we

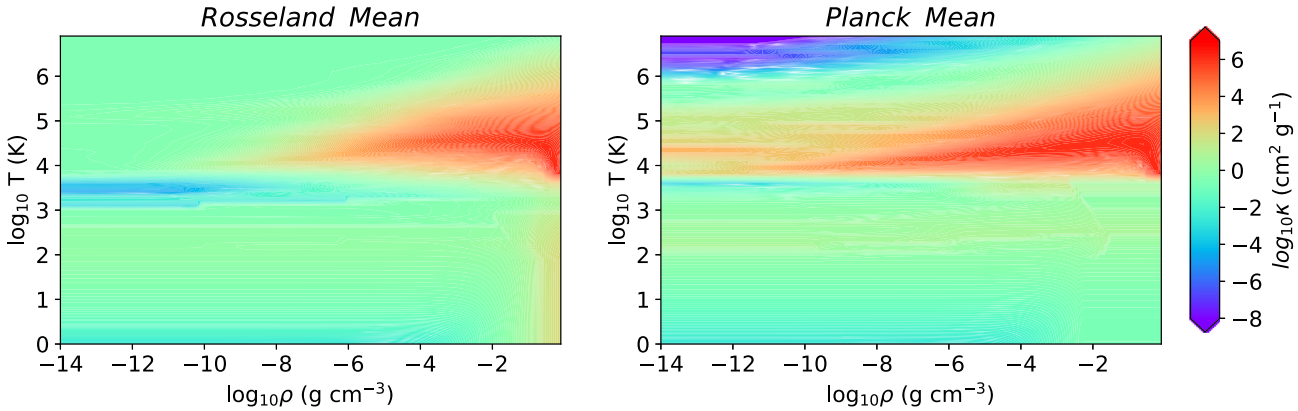

Figure 3. The final combined Rosseland mean and Planck mean opacities.

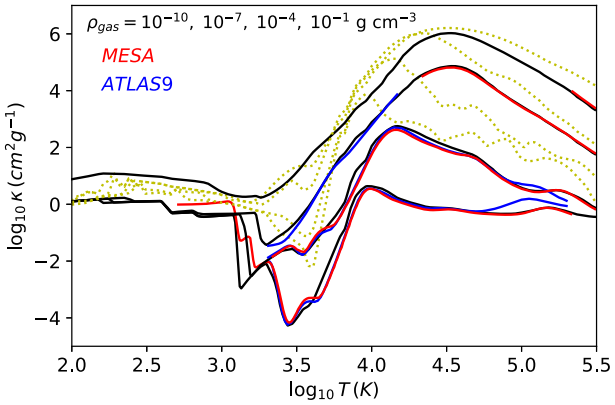

Figure 4. Our combined Rosseland mean (black curves) and Planck mean (yellow dotted curves) opacities compared with the MESA and ATLAS9 Rosseland mean opacities at different gas densities and temperatures. Only the opacities at their valid $\rho - T$ conditions are plotted. In the common $\rho - T$ parameter space where different opacity data bases are all valid, our opacities agree with the other opacities quite well.

can achieve a much better time-scale separation between the radiation transport and fluid dynamics. In most of our cases, the speed of light only needs to be reduced at most by a factor of 10 for the implicit method, compared with a factor of 2×10^5 for the explicit method. On the other hand, using the explicit and the implicit methods give almost identical results in our simulations, suggesting a good time-scale separation even for the explicit method. Test problems using either the implicit and explicit methods are provided in Section 3.2.1.

We adopt the third-order piecewise parabolic method (PPM) for spatial reconstruction for hydrodynamic quantities, which maintains a better hydrostatic equilibrium compared with the second-order reconstruction method. For the explicit radiative transfer, we also adopt the third-order spatial reconstruction for the intensity in the radiation transport step, which is crucial for accurately simulating regions with high optical depths (e.g. the optical depth of 10^4; Zhu et al. 2020). For the implicit radiative transfer scheme, the second-order intensity reconstruction is sufficient for capturing the thermal structure of the optically thick region, and is thus adopted. We use the second-order Van-Leer method for the time integration, and the HLLC Riemann solver to calculate the flux for hydrodynamic quantities.

3.1 Protoplanetary disc structure and planetary core properties

The protoplanetary disc structure determines the planet's atmosphere structure. For example, the disc temperature directly affects the envelope crossover time (Ali-Dib et al. 2020). Unlike most previous works (Lee et al. 2014; Piso & Youdin 2014) which use the minimum-mass solar nebula or the minimum-mass extrasolar nebula model (Chiang & Laughlin 2013), we adopt the disc structure from D'Alessio et al. (1998), which successfully fits protoplanetary disc observations. Its thermal structure is also self-consistently derived with disc radiative transfer calculations. We fit fig. 3 of D'Alessio et al. (1998) to derive the disc mid-plane temperature as

$$T_c = \begin{cases} 39.4 \times (R/10\,\mathrm{au})^{-4/5}\ \mathrm{K} & \text{if} \quad \mathrm{R} < 10\ \mathrm{au} \\ 39.4 \times (R/10\,\mathrm{au})^{-1/2}\ \mathrm{K} & \text{if} \quad \mathrm{R} > 10\ \mathrm{au}\,. \end{cases} \tag{2}$$

In the disc region beyond 10 au, stellar irradiation dominates. As in D'Alessio et al. (1998), we derive the disc surface density using the α disc model (Shakura & Sunyaev 1973). We also require the disc to be gravitationally stable. Thus, we have surface density $\Sigma = \min\{\dot{M}/(3\pi\nu), \Sigma_{Q=1}\}$, where $\nu = \alpha c_s^2/\Omega$ and $\Sigma_{Q=1} = c_s\Omega/(\pi G)$. We choose a constant accretion rate through the disc $\dot{M} = 10^{-8}\mathrm{M}_\odot\ \mathrm{yr}^{-1}$ and $\alpha = 10^{-3}$ for our disc model. Thus, at the disc radius $R = 5$ au, the disc's surface density is 488 g cm^{-2}, the mid-plane temperature is 66 K, the mid-plane density is 7×10^{-11} g cm^{-3}, and the disc's aspect ratio (H/R) is 0.037. With similar assumptions, our adopted disc model is similar to the Bitsch et al. (2015) model.

We choose 10 $M_\oplus$ as the planet's core mass in our simulations. Then, the Hill and Bondi radii for the planetary core at 5 au are

$$r_H = R\left(\frac{q}{3}\right)^{1/3} = 0.0216R = 0.58H\,, \tag{3}$$

where $q = M_p/M_*$. With our fiducial disc temperature,

$$r_B = \frac{GM_p}{c_s^2} = qR\frac{R^2}{H^2} = 0.0219R = 0.59H\,. \tag{4}$$

Both the Hill radius and the Bondi radius are about half of the disc scale height at 5 au. This is expected considering that the core mass of 10 $M_\oplus$ is close to the disc thermal mass

$$M_{th} = \frac{c_s^3}{G\Omega} = \left(\frac{H}{R}\right)^3 M_* = 17M_\oplus\,. \tag{5}$$

The radii r_B and r_H are related to the thermal mass with $r_B/H = M_p/M_{th}$, $r_H/H = 3^{-1/3}(M_p/M_{th})^{1/3}$, and $r_B/r_H = 3^{1/3}(M_p/M_{th})^{2/3}$. Thus, with $M_p \sim M_{th}$, we have $r_B \sim r_H \sim H$.

Table 1. Different setups for isolated-sphere and disc models.

	Fiducial	HighL	BigDust	HotDisc	LowL	LowLBD
$L/(1.54 \times 10^{-6} L_\odot)$	1	10	1	1	0.1	0.1
a_{max} for dust	1 mm	1 mm	10 cm	1 mm	1 mm	10cm
T_{irr}	66 K	66 K	66 K	174 K	66 K	66
t_{end}/t_p for 3D sphere	7.68	6.79	7.10	7.26	6.94	5.47
t_{end}/t_p for 3D disc	7.20	7.00	7.01	8.30	7.18	8.00

Knowing disc and planet properties, we should be able to study how Jupiter gathers its envelope in 3D simulations. However, the atmosphere build-up time-scale is the thermal (KH) time-scale, which is millions of years, much longer than our 3D simulations can afford. Instead, we can only study snapshots during the atmosphere accretion, similar to the static model discussed in the introduction. Then, we can connect different snapshots using the energy conservation as in the quasi-static model.

To simulate the envelope structure at one snapshot, we need to specify a luminosity throughout the envelope. The most important phase of Jupiter's atmosphere accretion is the phase when Jupiter is gathering its atmosphere mass to reach the crossover mass. This is also the longest phase during the atmosphere accretion, which directly determines if Jupiter can go through the run-away accretion. The luminosity during this phase can be estimated with $L = GM_p\dot{M}_p/r_p$, which is $L = 5.92 \times 10^{27}$ ergs s^{-1} (or 1.54×10^{-6} L$_\odot$) using $M_p = 10M_\oplus$, $\dot{M}_p = 10^{-5} M_\oplus\, yr^{-1}$, and $r_p = 2R_\oplus$. With this $\dot{M}_p$, a 10 $M_\oplus$ atmosphere can be accreted on to the $10M_\oplus$ core during the 1 Myr disc lifetime, so that run-away accretion can occur before the gas disc disperses. In reality, this luminosity is at the high end of the envelope accretion luminosity. It is more representing the beginning of the atmosphere gathering stage or the run-away accretion stage (Section 5.3). The actual accreted atmosphere is on top of the existing atmosphere so that not all the atmosphere is accreted to the core radius and we overestimate the energy released during the accretion. Furthermore, some protoplanetary discs' lifetimes can be 10 Myr so that a lower accretion rate can still trigger run-away accretion. Thus, we have also carried out simulations with 10 times less luminosity, which is $L = 5.92 \times 10^{26}$ ergs s^{-1} (or $1.54\times10^{-7}\, L_\odot$). We caution that a smaller luminosity leads to a colder and denser planetary atmosphere so that, after the initialization of the simulation, the atmosphere needs to collapse further to reach a steady state and this collapse takes a longer time. Within our simulation time (∼10 orbits), the atmospheres in these low luminosity simulations are not fully settled to steady states, as discussed in Section 4.1.

For our main simulations, we follow Pollack et al. (1996) and Rafikov (2006) to assume that the released energy is distributed throughout the envelope so that the luminosity actually follows (1-r_p/r)L. By replacing r_p with the inner boundary radius r_{in} (in our simulations r_{in} is ∼59 times r_p =2 $R_\oplus$; details in Section 3), this luminosity profile is also more numerically friendly since there is no large intensity close to the inner boundary. To achieve this luminosity, we add a heating rate to the whole envelope

$$\frac{\mathrm{d}E}{\mathrm{d}t} = \frac{L}{4\pi}\frac{r_{in}}{r^4}, \tag{6}$$

where E is the energy per unit volume. The resulting luminosity increases sharply from the inner boundary, and, for the bulk of the envelope, the luminosity is a constant, similar to the constant luminosity assumption in Piso & Youdin (2014). For our test case in Section 3.2.1, where we want to compare the simulation with the analytical solution, we indeed implement a constant flux inner boundary condition detailed in Appendix B.

After specifying the disc density, temperature, core mass, and core heating rate, we can simulate the planet's envelope in the disc. The envelope reaches a steady state with the given heating rate. We have tried six different setups (Table 1), including the fiducial case, the big dust case (thus lower opacity), the higher luminosity case, the hotter disc case, and two low luminosity cases that are identical to the fiducial case and the big dust case except for the low luminosity. These setups are summarized in Table 1. The BigDust setup explores how dust growth affects the envelope structure. The HotDisc setup simulates the giant planet formation in a hotter disc environment.

As will be shown in Section 4, convection directly affects the envelope structure. For a spherical envelope, the maximum luminosity that can be carried out by radiation before the envelope becomes unstable to convection is

$$L_{\max} = \frac{64\pi\sigma T^3}{3\kappa\rho(r)}\left(1-\frac{1}{\gamma}\right)\frac{\mu m_u G m(r)}{k_B}, \tag{7}$$

where m(r) is the mass within the radius r, $\rho(r)$ is the density at r, μ is the mean molecular weight, m_u is the atomic mass constant, and k_B is the Boltzmann constant. With T∼100 K in the outer envelope, m ∼ 10 $M_\oplus$, $\kappa \sim 1$ cm^2 g^{-1} for our fiducial opacity, $\rho_{\rm mid} = 7 \times 10^{-11}$ g cm^{-3}, $\gamma = 1.4$, and $\mu = 2.35$, we can derive $L_{\max} = 1.7 \times 10^{27}$ ergs s^{-1}. Since our fiducial luminosity is higher than this $L_{\max}$, the envelope in our fiducial case is convectively unstable. However, the BigDust case with $\kappa \sim 0.1$ cm^2 g^{-1} and the HotDisc case with $T_{\rm irr} \sim 174$ K have ∼10 times higher $L_{\max}$ that are larger than our provided fiducial luminosity. Thus, envelopes in these two cases should be radiative. Our low luminosity cases should also be radiative accordingly. These estimates are consistent with our simulation results in Section 4. Overall, by changing L, κ, and $T_{\rm irr}$, we can control the strength of convection in the envelope.

For each setup in Table 1, we carry out three simulations for comparison: the 1D radiation simulation for the isolated and spherical envelope, the 3D simulation for the isolated and spherical envelope (Section 3.2), and the 3D simulation for the planet envelope embedded in the disc (Section 3.3). We visualize these simulations in Fig. 5.

3.2 1D and 3D isolated sphere simulations

For the isolated spherical envelope, both 1D and 3D radiation simulations have been carried out to study the effect of convection. Our 1D radiation simulations have the radiative energy transport only. We do not add the energy transport due to convection from the sub-grid mixing-length theory. Thus, the 1D and 3D simulations have identical setups, and the only difference is that while 3D simulations allow convection, 1D simulations do not. If not specified, when we refer to 1D simulations, we mean 1D simulations with radiation only (no convection). Only in Section 5.1 where we develop a simple model for reproducing 3D simulation results, we consider convection in 1D models.

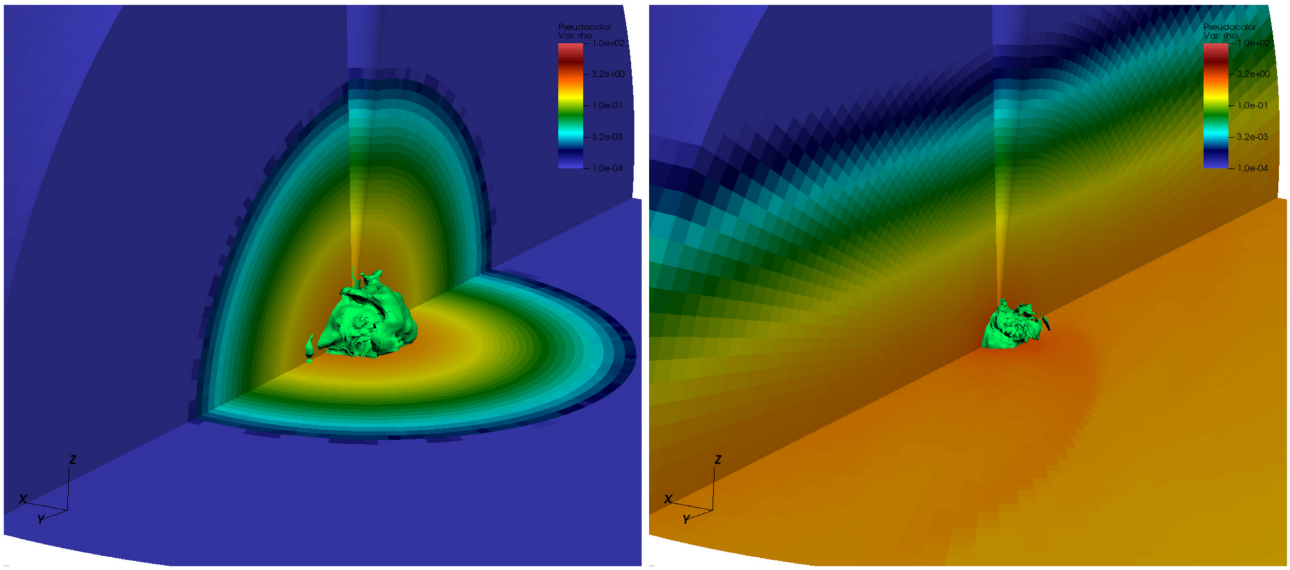

Figure 5. The density structure of the 3D isolated sphere (the left-hand panel) and 3D envelope-in-disc (the right-hand panel) simulations with our fiducial setup. The green surface at the centre is the iso-surface with a constant radial radiation flux. The iso-surface is not smooth due to the convective motion within the envelope.

The initial spherically symmetric envelope has a radial density profile of

$$\rho = \rho_0 e^{-r^2/2H^2}\,, \tag{8}$$

where $\rho_0 = 7 \times 10^{-11}$ g cm^{-3}, and H = 0.185 au, representing the vertical density stratification in the protoplanetary disc at 5 au, following our choice of disc parameters after equation (2).

To simulate the gravity from both the star and the planet, the envelope is subject to the gravitational force of

$$g(r) = \left(\frac{GM_p}{r^2} + r\Omega^2_{r=5\,\mathrm{au}}\right) \times f_s\,, \tag{9}$$

where $\Omega_{r=5\,\mathrm{au}}$ is the angular frequency of Jupiter's orbit. The first term on the right is the gravity from the planet, while the second term is the force component towards the disc mid-plane due to the stellar gravity. f_s is a smoothing function,

$$f_s = \frac{(r - r_{in})^2}{(r - r_{in})^2 + r_s^2}\,, \tag{10}$$

where r_{in} is the inner boundary of the simulation domain, and r_s is the gravitational smoothing length. With this smoothing function, the gravitational acceleration is zero at $r_{\rm in}$, which allows the disc to maintain a better hydrostatic equilibrium close to the inner boundary (Fung et al. 2019). Compared with previous 1D envelope calculations which start with the disc mid-plane quantities, our adopted gravitational force (equation 9) guarantees a much smoother transition from the planet envelope to the background disc. On the other hand, this setup is designed for simulating the vertical direction in the disc (perpendicular to the disc mid-plane), and it does not include the anisotropic density stratification in the disc and the disc's Keplerian shear. These shortcomings will be overcome by the disc setup in Section 3.3.

The initial condition is not in hydrostatic equilibrium since equation (8) does not take into account the gravity from the planet. After the planet gathers its envelope, the density structure beyond the planet's Hill radius should be smaller than the density from equation (8). However, in all our simulations, the planet's envelope mass within the Hill radius is at most 20 per cent of the total mass in the computational domain. Thus, the resulting density profile beyond the planet's Hill radius still follows equation (8) very well.

The 10 $M_\oplus$ core gathers envelope material quickly and reaches steady state during the thermal time ($C_v nT/L$), where C_v is the molar heat capacity and L is the typical luminosity. With the 0.3 $M_\oplus$ envelope (the typical envelope mass in our simulations) at our disc temperature and L being close to our fiducial luminosity (at early times, L is actually higher than our fiducial luminosity), the thermal time is ∼5 times Jupiter's orbital period. Note that this thermal time in the simulation is significantly shorter than the Myr KH time-scale of the planet's envelope since we only simulate the very outer region of the planet's envelope, which has low mass and low temperature. We run our simulations longer than the thermal time and ensure that the envelope has reached steady state (except for the low luminosity cases).

Our simulation domain covers r = 0.001 to 0.3 a_p with the Jupiter orbit's semimajor axis $a_p = 5$ au with 140 grid cells that are uniformly spaced in logarithmic space. The domain range is equivalent to 0.027–8.1 H at 5 au. The reflecting inner boundary and outflow (no inflow allowed) outer boundary conditions have been used in the radial direction. To guarantee that there is no mass flux at the inner boundary, we set the mass flux from the Riemann solver to be zero at the inner boundary. For 3D simulations, we have 40 grid cells uniformly spaced from $\theta = 0.1$ to $\pi/2$ in the poloidal direction, and 160 grid cells uniformly spaced from $\phi = 0$ to 2π in the azimuthal direction. We have adopted a reflecting boundary condition in the θ direction and a periodic boundary condition in the ϕ direction. The heat capacity ratio γ is chosen as 1.4 and the mean molecular weight is chosen as 2.35, considering that the gas mainly consists of molecular hydrogen at our studied density and temperature range. A global density floor of 10^{-10}–$10^{-8}\,\rho_0$ has normally been adopted. The smoothing parameter r_s for the gravitational force is chosen as 0.1 $r_{\rm in}$.

For radiative transfer calculations, we have used the angular discretization with respect to the local coordinate (r, θ, ϕ) in each cell. We have 8 longitudinal angles and 6 polar angles in the 3D simulations (a total of 96 discrete directions including both inward and outward directions) and 20 polar angles in the 1D simulations. At

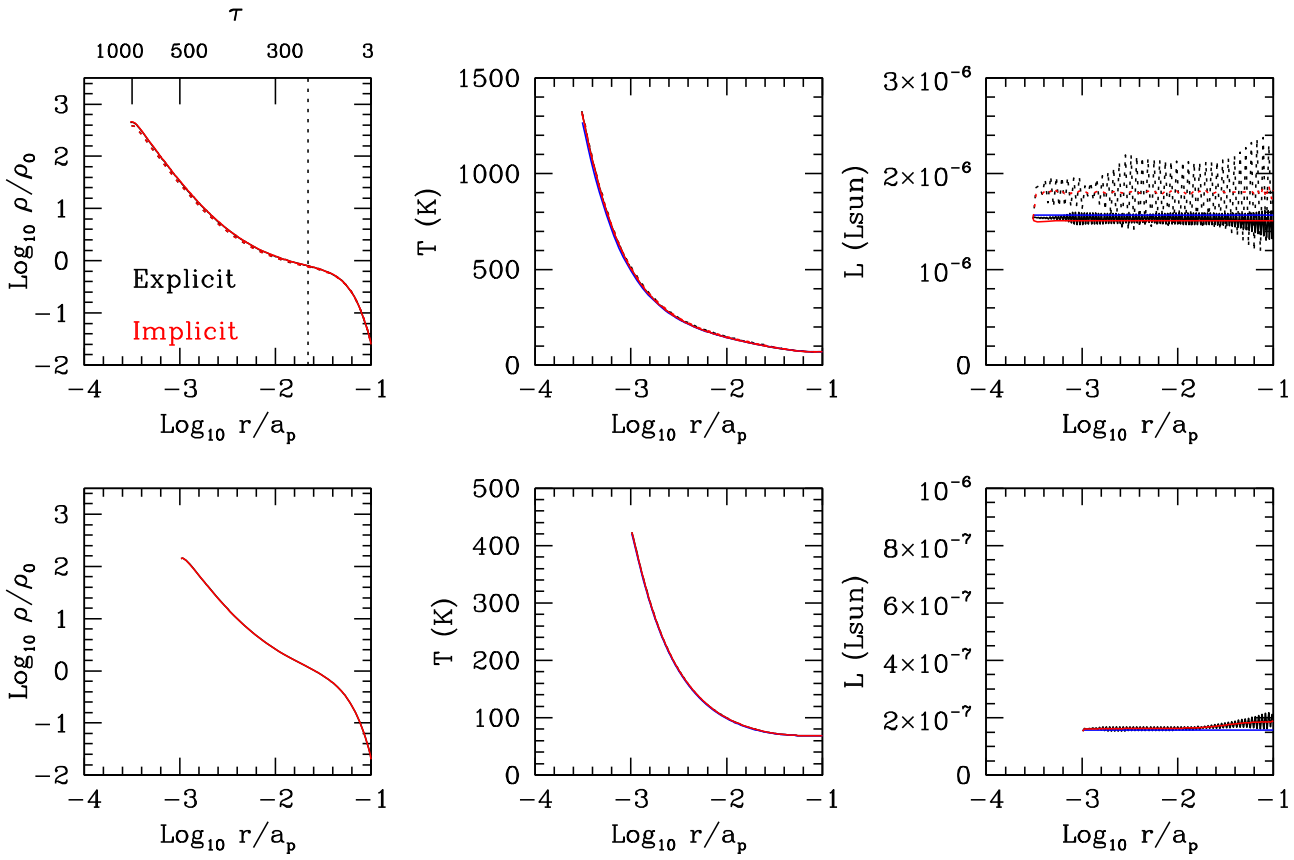

Figure 6. The density, temperature, and luminosity in our 1D envelope test problems with $r_{in} = 0.0003\,a_p$ (upper panels) and $r_{in} = 0.001\,a_p$ (lower panels). The black curves are from simulations with the explicit radiative transfer method, while the red curves are from simulations with the implicit radiative transfer method. The blue curves in the middle and right-hand panels are analytical solutions. In the upper panels, the dotted and solid curves represent low and high resolution runs, respectively. The vertical dashed line in the density panel labels r_H (which is also very close to r_B in this case).

the outer radial boundary, we assume that there is incoming isotropic radiation from the background medium (e.g. stellar irradiation) with a temperature of 66 K. With such a boundary condition, our simulation domain is kept at 66 K if there are no additional heating sources. The tolerance error is set at 10^{-5} for the implicit method.

3.2.1 Test problems

To explore the limitation of our grid setup and radiative transfer methods, we have done various slightly simplified 1D spherical simulations with different resolutions and radiative transfer methods, and compare them against the analytical results.

When the envelope is radiative, we can calculate the envelope's thermal structure analytically. For a steady state, the second momentum equation of the radiative transfer equation becomes

$$\nabla \cdot \boldsymbol{P}_r = -\kappa_T \rho \boldsymbol{F}_r \,, \tag{11}$$

where $\boldsymbol{P}_r$ and $\boldsymbol{F}_r$ are the radiation pressure tensor and the radiation flux, and κ_T is the total opacity. With the Eddington approximation, we have

$$\frac{1}{3}\frac{\partial E_r}{\partial r} = -\kappa_T \rho \frac{L}{4\pi r^2 c} \,. \tag{12}$$

where κ_T is the total opacity (including the absorption and scattering opacity) and c is the speed of light. With irradiation from a blackbody having a temperature of $T_{\rm irr}$, we use the two stream approximation to derive the temperature at the surface ($r = r_{\rm out}$, $\tau = 0$)

$$\frac{L}{4\pi r_{\rm out}^2} = F_r = \frac{c a_r}{\sqrt{3}} \left(T_{\tau=0}^4 - T_{\rm irr}^4\right) \,, \tag{13}$$

where a_r is the radiation density constant. With $E_r(\tau = 0) = a_r T_{\tau=0}^4$ as one boundary condition, we can integrate equation (12) from the surface at $r_{\rm out}$ to the interior at r to derive

$$T(r)^4 = \frac{3L}{4\pi c a_r} \int_r^{r_{\rm out}} \frac{\kappa_T \rho}{r^2} {\rm d}r + \frac{\sqrt{3}L}{4\pi R^2 c a_r} + T_{\rm irr}^4 \,. \tag{14}$$

The choice of $r_{\rm out}$ does not matter as long as the density drops sharply at large r so that the integral converges. We use our outer boundary $0.3\,a_p$ as $r_{\rm out}$ in our calculation below.

Fig. 6 shows various 1D test problems at t = 50 planetary orbits. In the lower panels, we adopt our fiducial grid setup as in Section 3.2 but with 1/10th of our fiducial luminosity (thus $1.54\times10^{-7}\,{\rm L}_\odot$, the same as our low luminosity cases). We use the constant radiation flux boundary condition at the inner boundary (the implementation is detailed in Appendix B) so that we can compare with the analytical solution of equation (14). Both the Planck and Rosseland mean opacities are chosen as 1 cm^2 g^{-1} for simplicity. All other parameters are the same as our fiducial cases in Section 3.2. The blue curve in the middle panel is from the analytical solution, which agrees well with our simulation results. After testing with various luminosities, we find that this luminosity is the lowest we can accurately simulate with our adopted grid setup. An even lower input luminosity will lead to a sharp density or pressure gradient close to the core, which will

generate significant artificial heating that can propagate throughout the whole envelope.

To demonstrate the artificial heating due to insufficient resolution, we carry out test simulations with a smaller $r_{in} = 0.0003 a_p$, as shown in the upper panels of Fig. 6. This leads to a sharper density or pressure gradient close to the core. We adopt our fiducial luminosity in these simulations. We carry out simulations with two different resolutions: 100 (dotted curves) and 200 (solid curves) radial grid cells uniformly spaced in logarithmic space. In the very inner region, where the pressure gradient is the largest, the limited number of numerical grid cells means that it is harder to maintain a good hydrostatic equilibrium, and a noticeable amount of extra heat is generated. In the rightmost panel, we can see that, when the resolution is low (100 grid cells), the real luminosity throughout the envelope is higher than our input luminosity from the inner boundary (the blue line). When we double the resolution, we can recover our input luminosity. Thus, high resolution is needed to simulate the region with a steep pressure gradient, or a larger smoothing length is needed. The red curves are from implicit methods, which show very similar results but with less variations.

Fundamentally, such numerical heating is a manifestation of insufficient numerical resolution at sharp density transition close to the inner boundary. The numerical scheme cannot maintain an infinitely sharp density transition. For example, we cannot simulate the whole atmosphere of a forming Jupiter if the atmosphere is isothermal, since the density contrast from the core surface at $r_{\rm core}$ to the Bondi radius is $exp(-(r_B - r_{\rm core})/h_{\rm core})$, where $(r_B - r_{\rm core})/h_{\rm core} = 1.7 \times 10^6$ with the envelope scale height ($h_{\rm core}$) calculated with our disc temperature. Trying to simulate this structure with insufficient resolution leads to a much smoother density profile. For our radiative transfer calculations, a smoother density profile close to the inner boundary corresponds to the density profile of a sphere with a higher luminosity. This higher luminosity can also be derived directly using the diffusion equation where a lower ρ leads to a higher luminosity with the same temperature structure. Thus, the smoother density profile manifests as numerical heating and higher luminosity. When we examine the velocity structure, we notice velocity fluctuations close to the inner boundary in the poorly balanced case, which drives the extra heating. It is difficult to give some specific rules on the numerical resolution needed. Different numerical schemes also provide different results (in our setup the PPM reconstruction behaves better than the piecewise linear PLM reconstruction). We also find that a larger smoothing length of the planetary potential can significantly reduce the numerical heating (as in Schulik et al. 2019), but it also limits the ability to simulate the innermost high density region. Thus, numerical resolution tests are crucial. Overall, with our fiducial setup ($r_{in} = 0.001\, a_p$), smoothing length ($r_s = 0.1\, r_{in}$), and luminosity ($\mathrm{L} = 1.54 \times 10^{-7}$ or $1.54 \times 10^{-6}\, \mathrm{L}_\odot$), we have confirmed that the numerical heating rate is significantly lower than our input luminosity.

3.3 3D disc simulations

After simulating the isolated envelope assuming the spherical geometry, we begin to simulate the planet's envelope in a background protoplanetary disc. Following the protoplanetary disc structure derived in Section 3.1, we set H/R = 0.037 at 5 au and a flat temperature radial profile. The mid-plane density at 5 au is $\rho_0 = 7 \times 10^{-11}$ g cm^{-3}, and it changes radially as $\rho_0 (R/5\ \mathrm{au})^{-3}$, where R is the distance to the star. The disc vertical structure is self-consistently determined by the vertical hydrostatic equilibrium, and the azimuthal velocity around the central star is also self-consistently determined by the radial force balance. Our simulation domain is centred around the planetary core at 5 au and is initiated with the background disc structure. Since the planetary core is orbiting around the central star, we need to consider non-inertial forces. The implementation of the non-inertial forces is given in Appendix A.

All parameters on the grid structure and boundary conditions are identical to our isolated sphere simulations in Section 3.2. The only differences in the setup are the outer radial boundary condition for fluid quantities and the initial condition using the disc structure (Fig. 5). Considering that the outer radial boundary is only 0.3×5 au away from the planet at 5 au, the central star and most of the disc are outside the whole computation domain centred around the planet. Thus, we need to feed the Keplerian flow at our radial boundary to maintain the disc structure. Thus, quantities at the outer boundary are always fixed with the disc's density, velocity, and energy as in the initial condition, which is similar to Zhu, Ju & Stone (2016).

4 RESULTS

We first present our results from 3D isolated sphere simulations (Section 4.1), and then present results from 3D disc simulations (Section 4.2). The 1D spherical simulations will also be compared with these 3D simulations.

4.1 3D isolated sphere simulations

After running the 3D isolated sphere simulations for several planetary orbits (Table 1), we present the envelope structure at $\theta = \pi/2$ plane in Fig. 7. For our fiducial case, despite the fact that the density and temperature structures are very axisymmetric, there is strong subsonic convective motion in the envelope. As shown in the leftmost panels of Fig. 7, no visible asymmetric structure can be seen in the density and temperature panels. However, there is subsonic convective motion shown in the v_r panel with the local mach number less than 0.5.

Convective motion is driven by the high luminosity in the envelope. To study the effects of convection on the envelope structure, we plot the spherically averaged 1D profiles of various quantities for both the 1D and 3D simulations in Fig. 8. As shown in the $\nabla \equiv \mathrm{dln}T/\mathrm{dln}P$ panel, ∇ in the 1D simulation is actually higher than the adiabatic temperature gradient ∇_{ad} in order to transport the energy out by the radiative diffusion. The ∇_{ad} is equal to $(\gamma - 1)/\gamma$ for the ideal gas. Based on the Schwarzschild criterion, whenever ∇ is higher than ∇_{ad}, the gas is convectively unstable, and, since convection is extremely efficient at transporting energy out, the envelope remains to be marginally convectively stable or unstable having $\nabla = \nabla_{ad}$. However, 1D simulations do not allow convective motion, since one gas parcel that is under another gas parcel remains under in 1D simulations. In 2D or 3D simulations that gas parcel can move up through the second or third dimension. As shown in the ∇ panel, allowing the convective motion, the 3D spherical simulations exhibit the expected $\nabla \sim \nabla_{ad}$. This $\nabla \sim \nabla_{ad}$ holds all the way from the centre to $log_{10}(r/5\ \mathrm{au}) \sim -1.5$, indicating that convection even reaches out beyond r_B (labelled by the vertical dashed line). In this paper, we define entropy per particle as

$$\mathrm{Entropy} = k_B ln \left(\frac{T^{\frac{\gamma}{\gamma-1}}}{P} \right) . \tag{15}$$

The entropy is shown in the upper right panel of Fig. 8 and the curve is flat in the convective region, as expected.

Convection is carrying part of the energy out from the interior to the surface. The radiative flux (F_r) and convective energy flux ($\langle E_g v_r \rangle$ where E_g is the internal energy density) are shown in the lower left

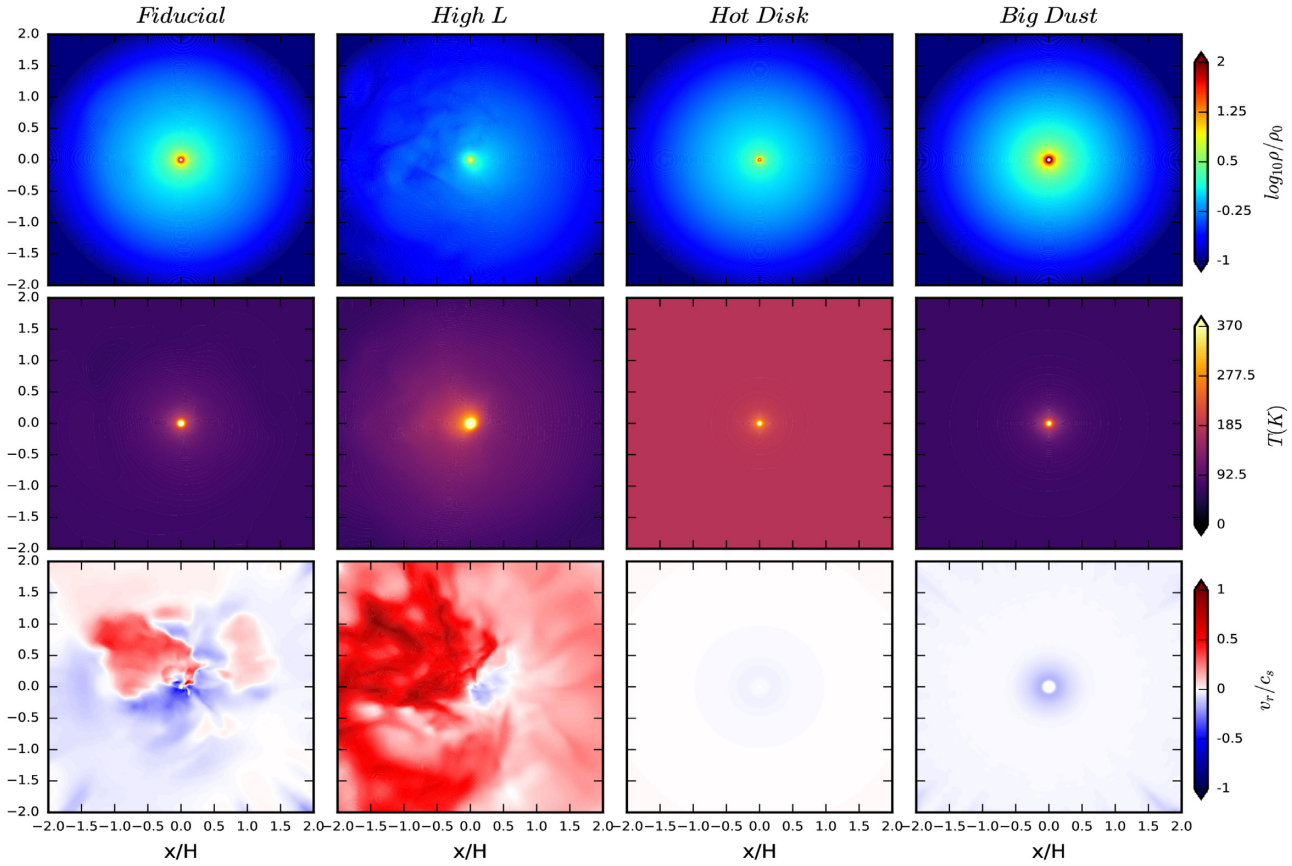

Figure 7. The density (upper panels), temperature (middle panels), and v_r (normalized to the local sound speed, lower panels) for four 3D isolated sphere models at the $\theta = \pi/2$ plane at the end of each simulation. Convection in the HighL case is so strong that we adjust the v_r/c_s colourbar for the HighL case to $[-2, 2]$. The left two models show convection, while the right two models do not show convection.

panel of Fig. 8. By comparing the 3D isolated sphere simulation with the 1D simulation, we can see that, in the 3D isolated sphere simulation, almost half the energy is carried out by convection and the other half by radiative diffusion. If we add the radiative and convective flux together, we roughly recover the green curve within r_B.

The presence of convection significantly changes the envelope's density and temperature structure. By comparing the 1D and 3D isolated sphere simulations, we can see that convection in 3D simulations makes the envelope colder and denser. By convectively transporting the energy out, the disc does not need to be very hot to transport heat out radiatively. The cooler envelope makes the envelope collapse more, leading to a higher density. In this case, the whole envelope is convectively unstable in our simulation domain.

After understanding the results for our fiducial case, we can study how different envelope parameters affect the envelope structure. As shown in Fig. 7, the higher luminosity in 'HighL' drives a much stronger convection. The colourbar for $v_r/c_{s,0}$ is adjusted to $[-2,2]$ accordingly, and we can clearly see that the turbulence becomes transonic. Such transonic motion does not provide enough time for the envelope to adjust itself from the turbulent motion. Thus, the density and temperature structure is not axisymmetric. We can clearly see turbulent features in the ρ and T panels. In the left-hand panels of Fig. 9, we see similar behaviour as the fiducial case. In the 1D model, ∇ is larger than ∇_{ad}, while in the 3D model convection tries to drive it back to ∇_{ad}. We notice that the actual ∇ is a little bit higher than ∇_{ad}. We think this might be due to the fact that, with such a high luminosity, even convection cannot transport energy out efficiently enough considering that the convective motion is already transonic. The convective envelope is again colder and denser in the 3D model compared with the 1D radiative model.

On the other hand, we can make the envelope less convective or even radiative by using either a hotter disc, a lower opacity, or a lower luminosity as discussed after equation (7). As shown in Fig. 7, the envelope structure is indeed axisymmetric and quiescent in the hotter disc or with the low opacity (from the bigger dust in the envelope). Most importantly, due to the spherical symmetry and the lack of motion, the envelope structure is almost identical between 1D and 3D isolated sphere simulations. This is demonstrated in the middle and right columns of Fig. 9, where the green and blue curves perfectly overlap with each other in these radiative envelopes. The ∇ is smaller than ∇_{ad} everywhere for both the 1D and 3D models. The convective flux is also significantly smaller than the radiative flux, again confirming that the envelope is convectively stable. Due to the radiative envelopes with $\nabla < \nabla_{ad}$, the entropy decreases towards the centre (middle rows of Fig. 9).

Overall, the 1D and 3D isolated sphere models produce identical envelope structure for the radiative envelope, but they produce different structures for the convective envelope since 1D simulations do not allow convection. On the other hand, if we include the effects of convection (e.g. $\nabla = \nabla_{ad}$) in the 1D semi-analytical model, we can reproduce the envelope structure in the 3D spherical simulations using 1D models, which will be studied in Section 5.1.

We also plot the 1D profiles of the lower luminosity cases in Fig. 10. The envelopes are mostly radiative. Even in 1D radiative

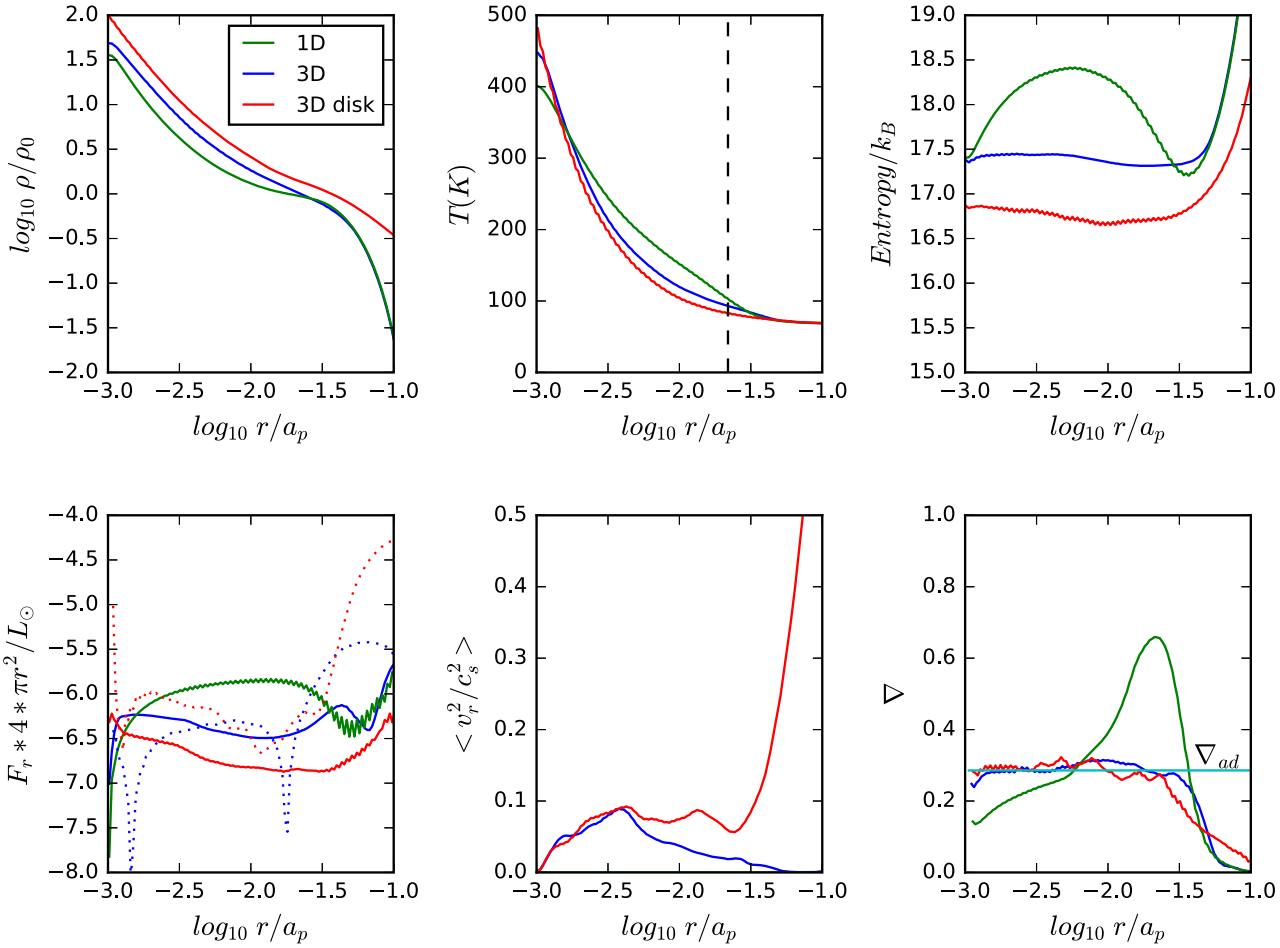

Figure 8. The radial profiles of various quantities for 1D (green curves), 3D isolated sphere (blue curves), and 3D disc (red curves) models with our fiducial setup. All quantities are spherically averaged over grids, except for the lower left panel which shows the spherically integrated energy flux (solid curves: radiative fluxes, dotted curves: convective fluxes from $E_g v_r$). The energy fluxes have been averaged over 20 snapshots over a time span of 0.2 planetary orbits. The energy fluxes, together with the pressure and temperature used in the lower right panel, have also been smoothed over 4 radial grids. The vertical dashed line in the temperature panel labels r_H (which is also very close to r_B in our fiducial case). Clearly, convection is prohibited in the 1D model so that ∇ can be higher than ∇_{ad}.

simulations, ∇ is smaller than ∇_{ad} in most regions, except for a narrow r range in the LowL case, where ∇ is barely higher than ∇_{ad}. Since the envelopes are radiative, 1D and 3D isolated sphere simulations are almost identical. On the other hand, the envelopes have not fully reached steady states with such a low luminosity (especially for the LowLBD case). The envelopes are still contracting with significant v_r so that the convective flux ($E_g v_r$) is still high. The radiative flux in the LowLBD case is still higher than our input flux of 1.54×10^{-7} $L_\odot$. The radiative flux is actually close to the convective flux suggesting that the energy increase due to the contraction is mostly radiated away. Longer 1D radiative simulations suggest that steady states (when the contraction stops) can be reached at t $\sim$ 20 planetary orbits (20 t_p).

4.2 3D disc simulations

Due to the Keplerian shear, the 3D disc simulations exhibit spiral arms that extend from the planet. We can see density concentration along the spirals in the upper panels of Fig. 11. These spirals can also perturb the disc's velocity structure (Rabago & Zhu 2021), as shown in the lower panels of Fig. 11, where the velocity perturbation (δv_r) suddenly changes sign along the spirals at y/H $= \pm 1$ when x/H $= \pm 2$. Goodman & Rafikov (2001) pointed out that the strength of a spiral is mainly determined by the mass ratio between the planet mass and the disc thermal mass (M_p/M_{th}). For the Fiducial and the BigDust models, their disc temperatures are the same and thus M_p/M_{th} is also the same. Then, their amplitudes of velocity perturbation at the spirals should also be similar, as shown in Fig. 11 (the leftmost and rightmost bottom panels). For the HotDisc model, M_{th}, which is proportional to c_s^3, is a lot higher so that M_p/M_{th} is a lot smaller than our fiducial case. Thus, the excited spirals are much weaker, demonstrated as the less apparent spirals in the ρ panel and smaller $\delta v_r/c_{s,0}$ in the velocity panel. Besides the spirals, we can also see the planet-induced horseshoe orbit at x/H $\sim \pm 0.5$ when y/H $= \pm 2$.

On the other hand, the envelope structure is very similar between the 3D isolated sphere and the 3D disc models. For our fiducial case, the envelope is also convectively unstable and $\nabla \sim \nabla_{ad}$, as shown in the ∇ panel of Fig. 8. For the convective envelope, the main difference between the 3D isolated sphere and disc models is that the 3D disc model has a slightly colder and denser envelope. This is partly due to the disc geometry, which leads to a higher density after the spherical-averaging (e.g. at r/5au $= 0.1$, the disc model has a higher density.). The higher averaged density with the same disc temperature leads to a lower entropy compared with the isolated sphere model at large r (shown in the entropy panel). Since a convective envelope in 3D tries to maintain a constant entropy throughout the envelope (even

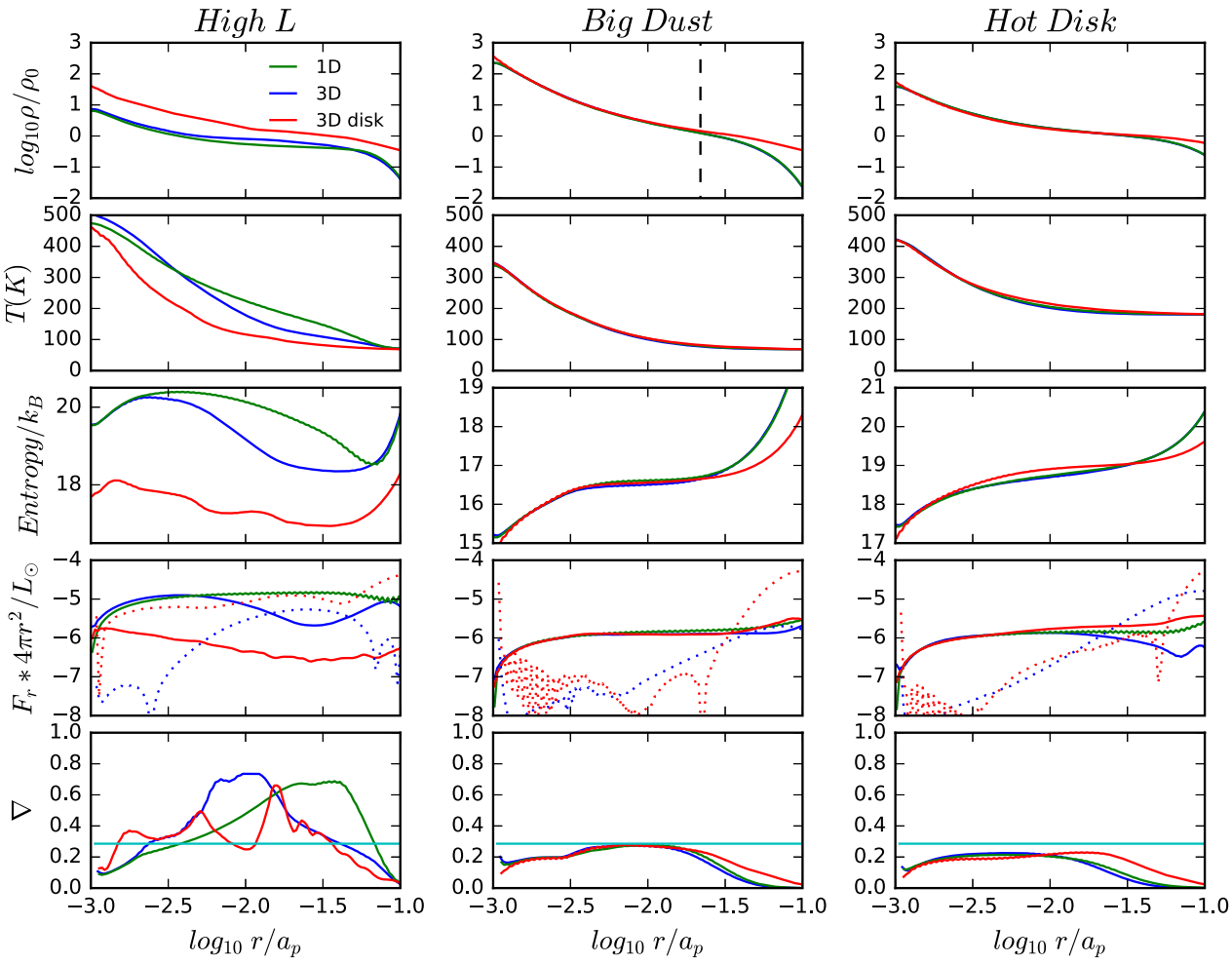

Figure 9. Similar to Fig. 8 but for three other setups.

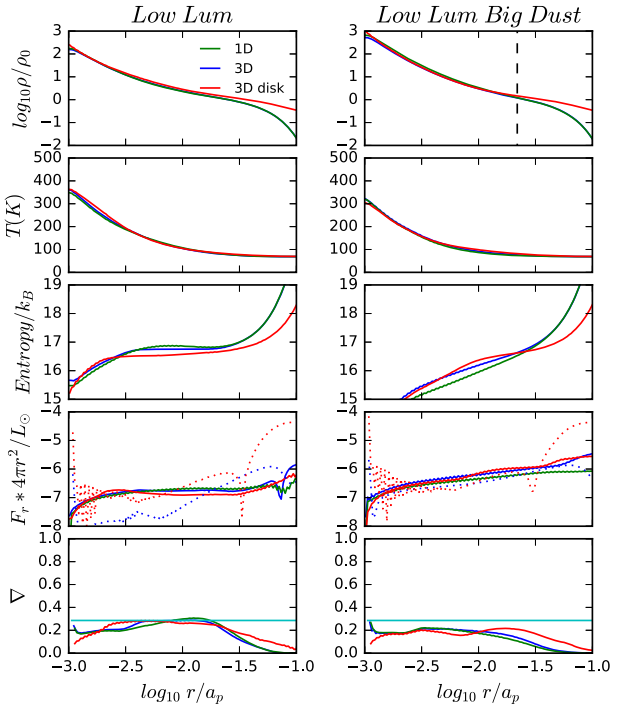

Figure 10. Similar to Fig. 9 but for two lower luminosity setups.

beyond r_B), the envelope's entropy in a 3D disc is lower than that in a 3D sphere. Another factor, which may be even more important, is that the convective motion in the isolated sphere seems to extend to larger r than that in the disc model. This can be seen in the bottom left panel of Fig. 7, where the convective motion extends to the scale of the disc scale height. The ∇ panel in Fig. 8 also shows that the $\nabla \sim \nabla_{ad}$ region extends to a slightly larger r in the 3D isolated sphere. Thus, the 3D isolated sphere maintains a high entropy from the surface. On the other hand, the envelope in a 3D disc is colder with a lower entropy, which then leads to a higher density concentration. The higher density leads to a higher optical depth. The radiative diffusion equation suggests that the same temperature gradient leads to a smaller radiative energy flux in a more optical thick environment. Thus, compared with the 3D isolated sphere model, less energy in the disc model can be carried out by radiation and more energy is now carried out by convection, as shown in the lower left panel of Fig. 8. The density and temperature differences between isolated spheres and disc models can be accounted with our 1D simple semi-analytical model in Section 5.1.

For radiative envelopes, the envelope structure is almost identical among the 1D/3D isolated sphere and disc models, indicating that the disc geometry has little effect on the radiative envelope structure. As shown in the right two columns of Fig. 9, the red curves overlap the green and blue curves perfectly within r_B. At a larger r, the disc geometry leads to a higher spherically averaged density which then causes a lower entropy and a higher ∇ there. Unlike the

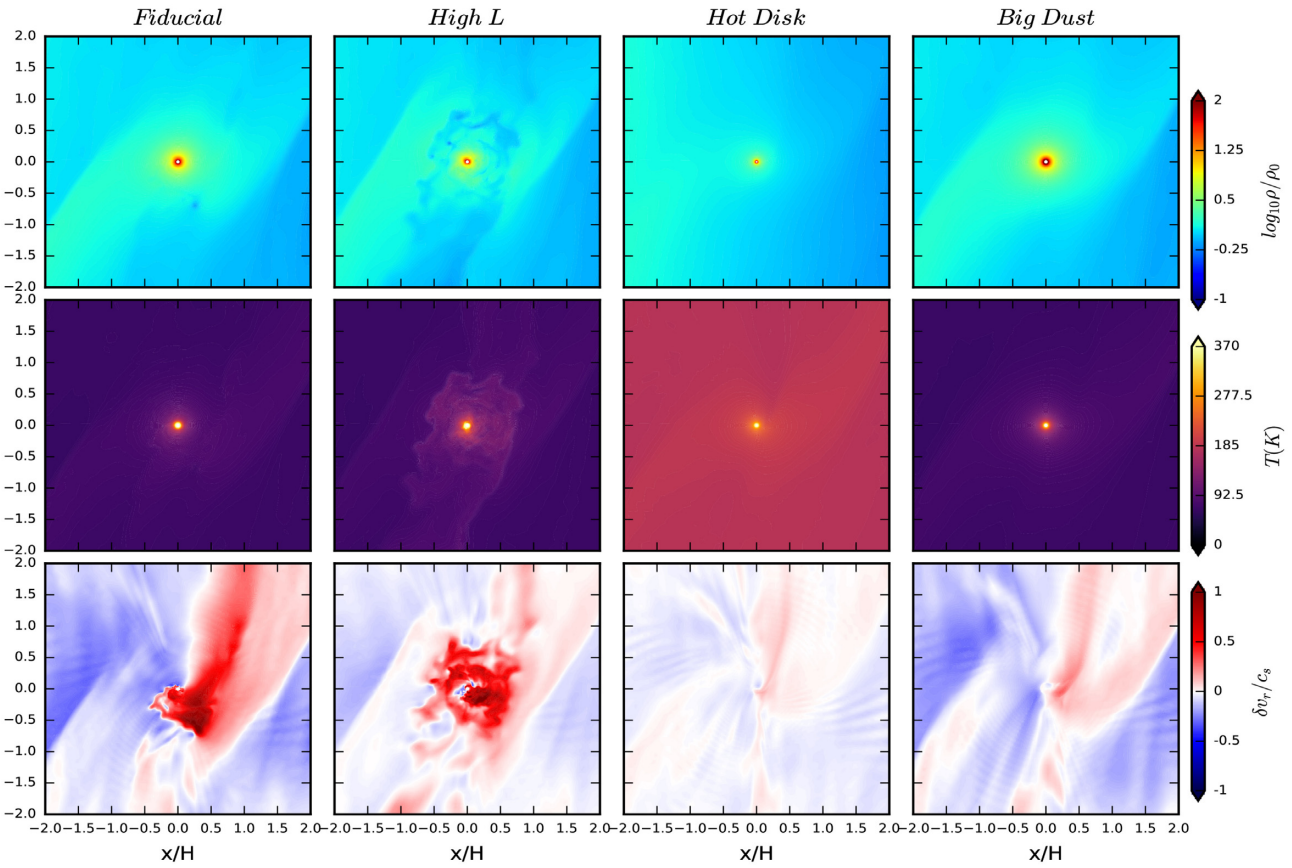

Figure 11. Similar to Fig. 7 but for 3D disc simulations. δv_r is the velocity difference between this snapshot and the initial condition (from the Keplerian shear). Again, convection in the HighL case is so strong that we adjust the $\delta v_r/c_s$ colourbar in the HighL case to $[-2, 2]$.

convective envelope, this higher density beyond r_B has little effect on the envelope structure. This is because the structure of a radiative envelope is determined by the temperature instead of the entropy in the disc, and the disc has quite a uniform temperature beyond r_B where the stellar irradiation determines the temperature structure. The photosphere of the envelope is quite high with our fiducial disc parameters. The photosphere is at ∼2.8 disc scale heights with our fiducial opacity, while the photosphere is at ∼2.1 disc scale heights with our big dust opacity.

4.3 Recycling

Such similarity between the isolated sphere and disc models for the radiative envelopes is quite surprising since we have observed significant net flow motion in disc models, as shown in the bottom panels of Fig. 11. Both the spirals and the horseshoe orbits in disc models lead to non-zero δv_r. Moreover the disc's Keplerian shear itself carries material in the envelope away.

To study how material within the envelope is recycled back into the disc, we add a passive scalar within $r/5$ au $= 0.05$ (roughly 2.5 r_B for the fiducial model) at $t = 5\ t_p$ when the envelope has already settled to a steady state. The passive scalar's initial density is the same as the envelope density at $t = 5\ t_p$. Then we continue the simulation for several orbits to see how the passive scalar is advected in the disc. Since no passive scalar is added into the domain after the initialization at $t = 5\ t_p$, the passive scalar is carried away by the disc flow and diluted. By tracing the evolution of the passive scalar, we can understand and quantify how mass is exchanged between the envelope region and the disc region.

Fig. 12 shows the evolution of the passive scalar at the disc mid-plane for the convective envelope (fiducial model in the upper panels) and the radiative envelope (BigDust model in the middle panels and HotDisc model in the bottom panels) after the passive scalar is injected at $t = 5\ t_p$. For the convective envelope, the convective motion quickly transports material near the centre to larger radii where it is carried away by the Keplerian shear. Within 2 orbits, almost all of the original envelope material is recycled into the disc. On the other hand, for the radiative envelope, even though the outer envelope is recycled, the inner core (within 0.1–0.2 r_H) is protected from the recycling. We note that the protected regions in the BigDust and the HotDisc models are both around 0.1–0.2 r_H, although r_H in the HotDisc model is $\sim 2.6 r_B$, while $r_H \sim r_B$ in the BigDust model.

To quantify the efficiency of the recycling, we integrate the mass, entropy, and internal energy of the passive scalar within a sphere of r_H, 0.2 r_H, and 0.1 r_H for three different models, and plot these quantities with time in Fig. 13. As shown in the upper left panel for the convective envelope, the total mass of the passive scalar decreases exponentially no matter where the mass is calculated. Within two planetary orbits, the mass has decreased by almost two orders of magnitude. The entropy and internal energy per unit mass is constant with time, indicating that the passive scalar is well mixed in the envelope and the mass is depleted at the same rate at different envelope regions. For the radiative envelopes shown in the right two columns, the passive scalar's mass within r_H decreases quickly, while the mass within 0.2 and 0.1 r_H (especially within 0.1 r_H) is almost a

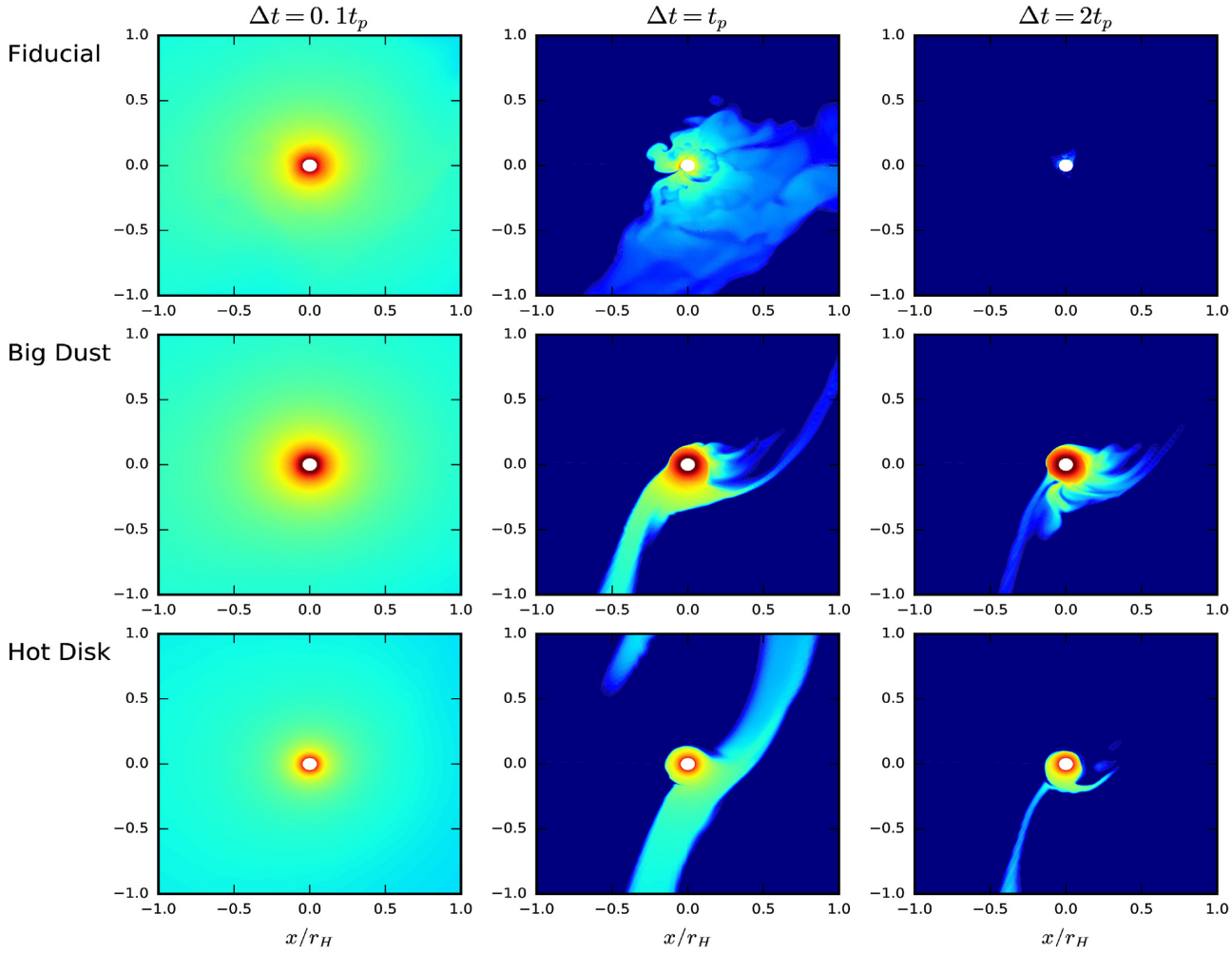

Figure 12. The evolution of the passive scalar at the disc mid-plane for the fiducial model (upper panels), the big dust model (middle panels), and the hot disc model (bottom panels) at different times (left-hand to right-hand panels) after the passive scalar is injected.

constant. The entropy or internal energy per unit mass decreases or increases with time (especially within the r_H sphere), indicating that the outer envelope where the entropy is the highest and the internal energy is the lowest has been recycled first.

The recycling pattern revealed by the passive scalar can also be directly probed with the velocity vectors within the envelope. Fig. 14 shows the velocity vectors for both isolated sphere and disc simulations. The vectors in all the panels are on the same scale. The left two panels show the convective envelopes, where we can clearly see the rolling motion at various scales. The right two panels show that the radiative envelopes have much slower motion. Even though the lower right panel (the disc model) shows slightly faster motion than the upper right panel (the sphere model), the radial flow in the disc model decreases dramatically around the core at 0.07 H ($\sim$0.12 r_H). This is consistent with our passive scalar results that, for radiative envelopes, the region within 0.1–0.2 r_H is protected against recycling. Although the global flow pattern is less robust in our local simulations which centred around the planet instead of the star, the global simulations from Fung et al. (2019) also reveal that the flow velocity decreases dramatically at similar scales.

The protected inner core could be qualitatively understood using the buoyancy force argument. When the gas parcel is moving towards the planet due to the planet's gravity (e.g. the Meridional flow), it is against the buoyancy force from a thermally stable atmosphere. Thus, it is slowed down and eventually stopped. Since the thermal effect plays a role here, we expect that the slowing down occurs when the entropy of the envelope is smaller than the disc entropy at the disc scale height. Fig. 9 shows that the entropy starts to decrease sharply at 0.2 r_H for the radiative envelopes. Another way of thinking is that the infalling material stops at the position where its ramp pressure balances the thermal pressure. For a transonic inflow, this occurs when the envelope temperature becomes significantly higher than the disc temperature.

5 DISCUSSION

5.1 New procedures for 1D semi-analytical models

Based on results from our direct 3D simulations, we can improve previous 1D models for calculating the envelope's structure, mainly regarding the outer boundary condition in the 1D models. Previous approaches use the minimum of the planet's Hill radius and Bondi radius as the outer boundary for 1D calculations (e.g. Bodenheimer & Pollack 1986). The disc mid-plane density and temperature are used as the outer boundaries' density and temperature. Recently, a much

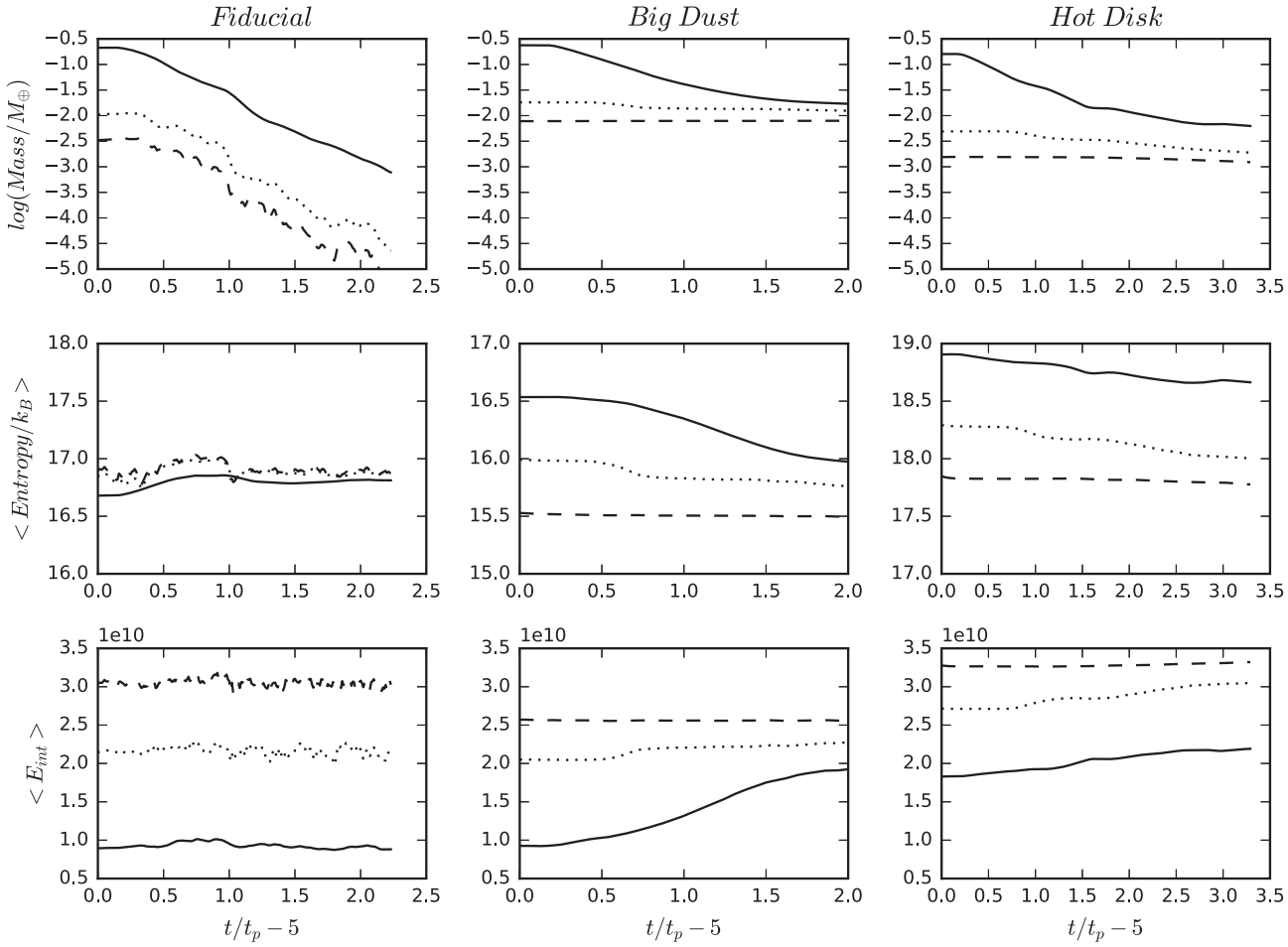

Figure 13. The time evolution of the passive scalar after being injected around the planet for three different disc models (left-hand to right-hand panels). The upper, middle, and lower panels show the integrated mass, the spherically averaged entropy, and the averaged internal energy per unit mass within a sphere of r_B (solid curves), $r_B/5$ (dotted curves), and $r_B/10$ (dashed curves).

smaller radius (e.g. 1/5–1/3 of the Bondi radius) has been used as the outer boundary in 1D calculations (e.g. Lee 2019; Ali-Dib et al. 2020), where the entropy is set to be the same as the disc's entropy. This is motivated by 3D simulations in which material beyond that radius is recycled to the disc. For the fully convective envelope, the outer boundary position does not matter since the envelope's entropy is the same as the disc's entropy anyway. However, for radiative envelopes, our 3D simulations do not support such a small radius approach at least for the planetary core at 5 au. For the radiative envelopes shown in Fig. 9, ∇ is smaller than ∇_{ad} throughout the whole region. There is no constant entropy region beyond 0.1–0.2 r_B. The density and temperature profiles are almost identical to those in the isolated sphere calculations. Recycling does happen (as in Section 4.3), but the time-scale of recycling is longer than the thermal time-scale of recycled material (Section 5.2). Thus, the temperature structure is hardly affected by the recycling and is similar to that of an isolated sphere.

Considering that the planet's gravity does not abruptly stop at the Hill or Bondi radius, we choose a larger radius, the disc scale height, as the outer boundary condition. The spherically averaged density there is

$$\rho = 1.33\rho_{\rm mid}e^{-1/2} = 0.81\rho_{\rm mid}\,, \tag{16}$$

where the factor of 1.33 accounts for spherically averaging the flat disc density structure in every direction at r = H from the planet (e.g. in the mid-plane, the density is still the mid-plane density at r = H). The temperature there is chosen as either the disc mid-plane temperature (if the envelope is convective at r = H) or the temperature derived with equation (14) integrating from the disc surface to r = H (if the envelope is radiative at r = H). Finally, starting with these density and pressure at r = H, we integrate from r = H towards the core with both the disc's and the planet's gravity (equation 9 with $f_s = 1$) to derive the envelope structure. Similar to the traditional approach, ∇ is calculated with the thermal diffusion equation, and we switch to $\nabla = \nabla_{ad}$ whenever $\nabla > \nabla_{ad}$. Compared with our 3D radiation hydrodynamical simulations, this approach is significantly simpler and faster and we refer it as the 1D semi-analytical model.

The resulting envelope structures using our fiducial opacity and $a_{\rm max} = 10$ cm opacity are shown in Fig. 15 as the dashed curves. We can see good agreement between this simple semi-analytical model and 3D simulations for both the convective (left-hand panels) and the radiative (right-hand panels) cases. At the outer boundary, the density is slightly higher in 3D simulations since even the disc region beyond r = H still feels the planet's gravity and concentrates slightly.

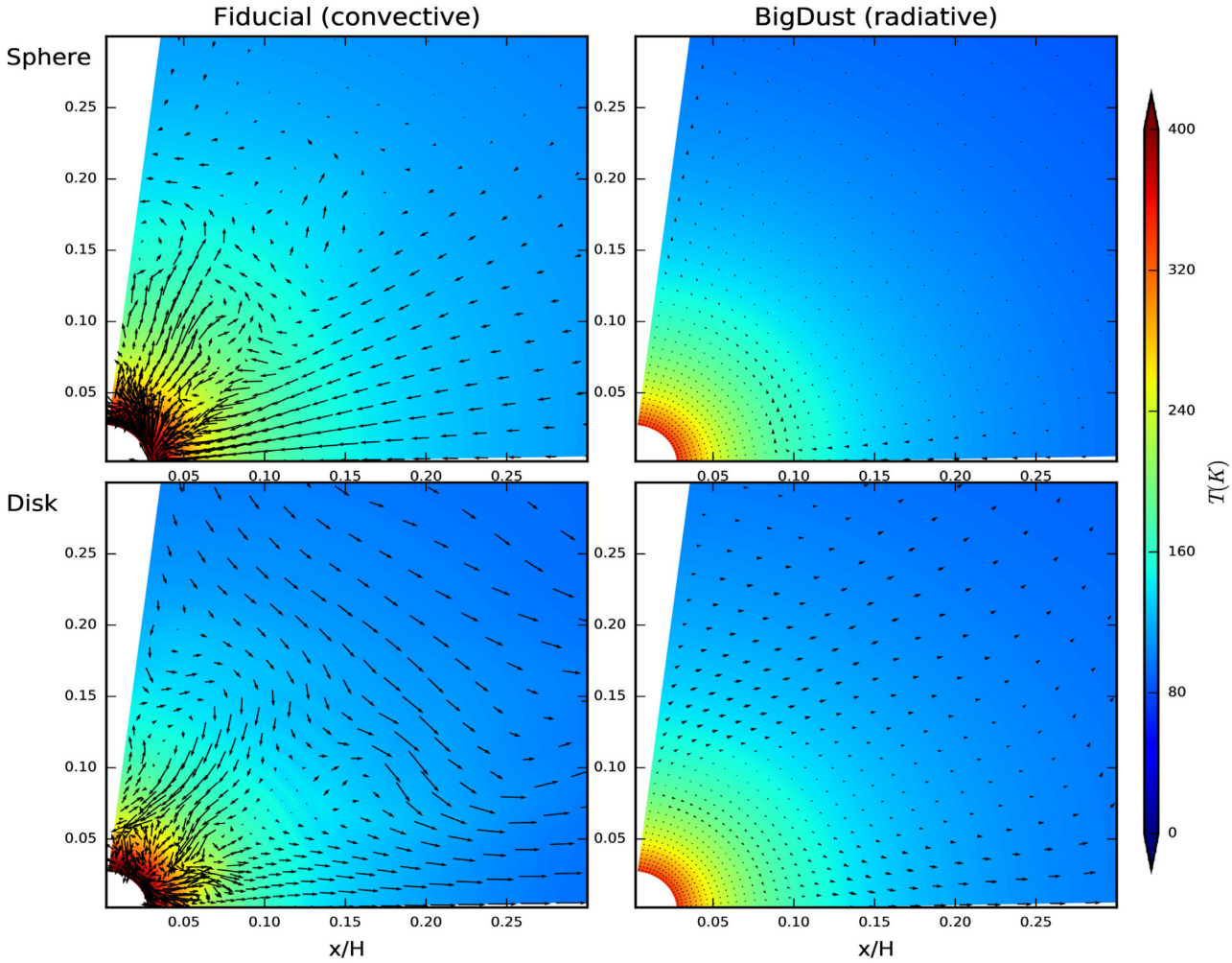

Figure 14. The vertical slices of the temperature structure in 3D isolated sphere models (upper panels) and 3D disc models (lower panels) for the fiducial setup (left-hand panels) and BigDust setup (right-hand panels) in the direction away from the star. In the disc models, the slices are from the direction that is pointing towards the central star. The lengths of the velocity vectors are on the same scale among all the four panels.

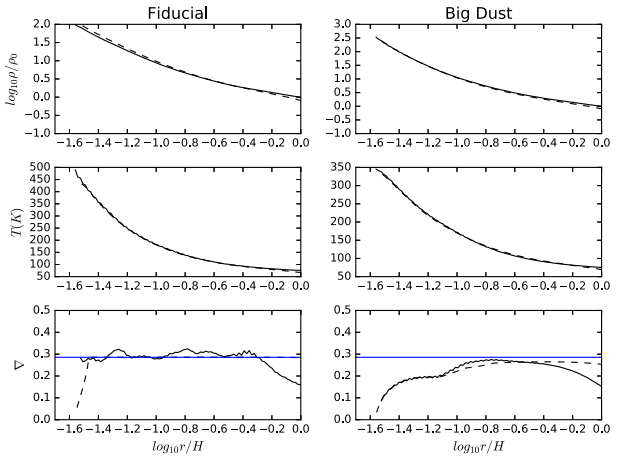

Figure 15. The envelopes' structure in 3D simulations (solid curves) and 1D semi-analytical models (dashed curves) of Section 5.1 for both the convective (left-hand panels) and radiative (right-hand panels) envelopes. The blue line in the ∇ panel represents ∇_{ad}.

5.2 Various time-scales

The planet's atmosphere or envelope accretion involves dramatically different spatial scales (e.g. core and disc scales) and time-scales (e.g. recycling and KH time-scales). The structure of the envelope largely depends on the relative amplitudes among these scales. Unfortunately, direct numerical simulations can only simulate very limited spatial and time-scales. Thus, it is important to estimate the various time-scales for the entire envelope. Particularly, we want to compare the recycled material's cooling time-scale with the recycling time-scale to understand if the recycling process can affect the envelope's thermal structure.

Cooling time-scales are the ratio of energy content to an energy loss rate. The cooling time for an entire bound object is a KH time-scale, *E*/*L*, where due to the virial theorem it is most correct to use total energy, but (also by the virial theorem) either the thermal or gravitational energy is usually a good approximation. To estimate the cooling time-scale, we use our 1D semi-analytical model in Section 5.1 to calculate the planet's envelope structure all the way to the core (2 earth radii) with either the fiducial opacity or the big dust opacity. All other parameters, including the disc condition, the luminosity, and the adiabatic index, are the same as in our fiducial

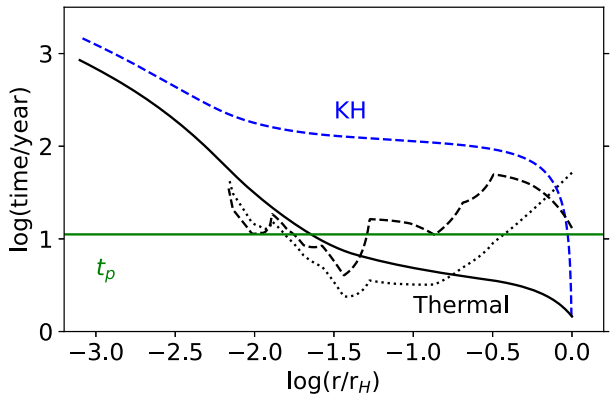

Figure 16. The KH time-scale (dashed blue curves), and the thermal time-scale for the recycled material (black curves) based on the 1D model with the big dust opacity. The horizontal dashed line represent the Jupiter's orbital time. The solid, dotted, and dashed black curves are different estimates for the thermal time-scale using different approximations (detailed in the text).

case. From the resulting structure, we integrate the thermal energy from the Hill radius inwards,

$$E_{\rm tot}(r) = \int_{r_H}^{r} E(r')4\pi r'^2 {\rm d}r' \tag{17}$$

where and $E(r')$ is the energy per unit volume at r'. Then, we use $E_{\rm tot}(r)/L$ to derive the KH time-scale at different r in the envelope. It represents the time-scale for the given luminosity to affect the thermal energy of the envelope material above r. This time-scale for the big opacity case is given in Fig. 16 as the blue dashed curve. This is the longest time-scale in the process of envelope accretion. We note that our KH time-scale at the core is only 10^3 yr, significantly shorter than the Myr KH time-scale normally assumed in the Jupiter's atmosphere accretion. This is mainly due to our assumed high luminosity. As discussed in Section 3.1, our fiducial luminosity is ∼10 times higher than the typical envelope's luminosity during the contraction. This high luminosity not only transports the energy out quicker, but also leads to a hotter and less massive envelope. Both effects decrease the KH time-scale in our models. On the other hand, this KH time-scale is the whole envelope's cooling and contraction time-scale, which is not the recycled material's cooling time-scale.

Cooling times for the recycled material can be derived using the cooling times for local thermal perturbations. We recap this time-scale for the case of optically thick perturbations larger than $\ell_\lambda = (\kappa\rho)^{-1}$. For a thermal perturbaton δT on length-scale ℓ_x in a plane-parallel atmosphere, the excess energy per volume is $\rho c_V \delta T$ with c_V the specific heat per unit mass. The energy loss per volume is $\nabla \cdot F \sim \delta F/\ell_x$. The radiative flux is $F = k_{\rm rad}\nabla T$ with $k_{\rm rad} = 16\sigma T^3/(3\kappa\rho)$. Thus $\delta F \sim k_{\rm rad}\delta T/\ell_x$ and

$$t_{\rm cool} \sim \frac{3c_V\rho^2\kappa}{16\sigma T^3}\ell_x^2 \tag{18}$$

in agreement with standard expressions (in the diffusive regime). We can use this cooling time-scale to describe cooling during the 'atmospheric recycling' process.

'Atmospheric recycling', i.e. the flow of disc gas inside the envelope of a protoplanet (i.e. inside its Bondi radius) can limit the cooling of a protoplanet by constantly delivering disc material which has a higher entropy than any parts of the envelope that have already cooled. The existence of the radiative envelopes in some simulations reveal that in regions with recycling the envelope still has a stably stratified, radiative structure with $\nabla < \nabla_{\rm ad}$. Furthermore, ∇ in these 3D radiative envelopes which are subject to recycling is almost identical to the ∇ in corresponding 1D radiative simulations, indicating that the recycled high entropy disc flows cool efficiently on their recycling time-scale. To quantify this we define the extra energy content that must be lost if the actual temperature T is below the adiabatic $T_{\rm ad}$ that has the disc entropy (at that radius and pressure).

$$E_{\rm extra} = 4\pi\int_r^{r_{\rm out}} \rho c_V (T_{\rm ad} - T) r'^2 {\rm d}r' \tag{19}$$

$$\simeq 4\pi\int_r^{r_{\rm out}} \rho c_V \left[\int_{r'}^{r_{\rm out}} (\nabla_{\rm ad} - \nabla)\frac{\mu g}{\mathcal{R}}{\rm d}r'\right] r'^2 {\rm d}r', \tag{20}$$

where we use $T = T_o(r_{\rm out}) - \int {\rm d}T/{\rm d}r{\rm d}r = T_o + \int \nabla\mu g/\mathcal{R}{\rm d}r$, with an ideal gas law $P = \rho\mathcal{R}T/\mu$, the hydrostatic equilibrium ${\rm d}P/{\rm d}r = \rho g$, and similarly for $T_{\rm ad}$. We further approximate the integral as

$$E_{\rm extra} \sim 4\pi c_V \rho T r^3 (\nabla_{\rm ad} - \nabla), \tag{21}$$

which could be too severe an approximation. It assumes that $\int_r g{\rm d}r \sim GM_{\rm p}/r$ and that the density integral is dominated by the deepest $H_{\rm p} = P/(\rho g)$.

The available luminosity to carry away this $E_{\rm extra}$ is likely not the entire luminosity as usual sources of luminosity (KH contraction and planetesimal heating) are not responsible for this additional cooling of the recycling flows. Moreover, there is likely no additional luminosity to easily measure in a numerical model, if it is in a quasi-steady state. Given these issues, the relevant luminosity is best defined relative to $E_{\rm extra}$ as the additional luminosity that would be generated by an adiabatic envelope, i.e.

$$L_{\rm extra} = \frac{64\pi\sigma T^4 G m(r)}{3\kappa P}(\nabla_{\rm ad} - \nabla) \tag{22}$$

$$= \frac{64\pi\sigma T^4 r^2}{3\tau_\parallel}(\nabla_{\rm ad} - \nabla), \tag{23}$$

where the final form uses the optical depth $\tau_\parallel = \kappa P/g$ that would apply in a plane-parallel atmosphere.

The resulting cooling time for recycling flows is then

$$t_{\rm crc} = \frac{E_{\rm extra}}{L_{\rm extra}} \sim \frac{15 P r \tau_\parallel}{32\sigma T^4}, \tag{24}$$

where the approximate expression uses equation (21) instead of equation (19) and the diatomic $c_V = 5/2\mathcal{R}/\mu$. If we compare to the standard equation (18) then

$$\frac{t_{\rm crc}}{t_{\rm cool}} = \frac{\tau_\parallel r}{\tau_x \ell_x}, \tag{25}$$

where $\tau_x = \rho\kappa\ell_x$ for the perturbation, so the only difference is in effective optical depths and length-scales.

Thus, we can estimate the cooling time for recycling flows using our derived 1D envelope structure. Fig. 16 shows these time estimates for the big dust opacity case. The solid black curve represents $E_{\rm extra}/L$ where $E_{\rm extra}$ is from equation (19) and L is the constant luminosity throughout the envelope. The dashed black curve uses the same $E_{\rm extra}$, but L is from equation (22) at different r. The dotted black curve is from equation (24). Overall, the cooling time-scale is comparable or shorter than the orbital time-scale (which is also the recycling time-scale) at $r > 0.01 r_H$. Thus, recycling has limited impact on the thermal structure of the envelope.

At the same time, the core and envelope can be convective (e.g. our fiducial opacity case). When the envelope is convective, the energy transport time-scale is the time-scale of the convective motion. The convection speed can be estimated using the Mixing-length-theory (MLT). However, the MLT requires us to solve the deviation of the envelope's temperature gradient from the adiabatic temperature

gradient, which is beyond our simple 1D model. Thus, we roughly estimate the convection velocity using the empirical relationship (Porter & Woodward 2000; Fuller 2017; Jones et al. 2017),

$$v_{\rm conv}(r) = \left(\frac{L}{4\pi r^2 \rho}\right)^{1/3}. \quad (26)$$

Using the 1D model with our fiducial setup, we can estimate $v_{\rm conv}(r)$. It turns out that $v_{\rm conv}(r)$ is roughly a constant throughout the envelope with the value of $\sim$0.1 $c_{s,0}$ where $c_{s,0}$ is the sound speed at the disc temperature. This is consistent with our simulations (Fig. 7). Thus, the convection time-scale ($r_H/(0.1\ c_{s,0}) \sim 6/\Omega$) is the orbital time-scale.

By comparing these time-scales, we can discuss the effect of recycling which occurs on the orbital time-scale (Section 4.3). For a convective envelope, the recycling time-scale is similar to the convective time-scale. Thus, recycling can quickly exchange the envelope material with the disc material even to the deepest part of the outermost convective envelope. In our fiducial 3D disc simulation, the convective envelope extends to our inner boundary, which explains why all the envelope material have been recycled efficiently. In our 1D semi-analytical model, there is a radiative zone from 0.005 r_H to 0.05 r_H separating the inner and outer convective regions so that the recycling may only be effective for the outer convective zone (>0.05 r_H).

For a radiative envelope, the mass recycling is only efficient beyond 0.1 r_H. Even so, the thermal structure of that outer region is hardly affected by the recycling process, implying that the thermal time-scale to establish the envelope's thermal structure is shorter than the recycling time-scale. Quantifying this thermal time-scale is difficult. Our crude estimate (black curves in Fig. 16) indeed suggests that the cooling time-scale is shorter or comparable to the recycling time-scale. Overall, for the planet at 5 au, the recycling has large effects on the mass exchange for the outer envelope, but it has limited effects on the thermal structure of the envelope. At 0.1 au where the orbital time-scale decreases dramatically, the recycling may have stronger effects on the envelope's thermal structure.

5.3 Jupiter's evolution

After calculating the envelope structure at different snapshots, we can use the energy conservation (e.g. Piso & Youdin 2014) to connect them and derive the time evolution of the Jupiter's envelope accretion. In detail, given an envelope mass, we search for the luminosity which can sustain this envelope, and derive the resulting envelope structure. Then, we calculate the energy difference between two snapshots having slightly different envelope masses, and divide this difference with the luminosity to calculate the time span between these two snapshots. Finally, connecting all the snapshots from small to large envelope masses, we can derive the time evolution of envelope accretion. Runaway accretion starts when the luminosity begins to increase with the increasing envelope mass, which normally occurs when the atmosphere mass roughly equals the core mass (the atmosphere reaches the cross-over mass). We have ignored the effects of mass and volume change on the energy equation, as in Lee et al. (2014). We use the new 1D models in Section 5.1 to calculate the envelope structure, but now with the full EOS from Piso & Youdin (2014) and the new opacity in Section 2. When we calculate the envelope's energy, we only include the envelope within 1/10th of the Hill radius since only this region is bound in our radiative envelopes. Fig. 17 shows the time evolution of the envelope-to-core mass ratio and the envelope luminosity for a 10 earth mass core at 5 au. The envelope mass only includes the envelope within 1/10th of the Hill

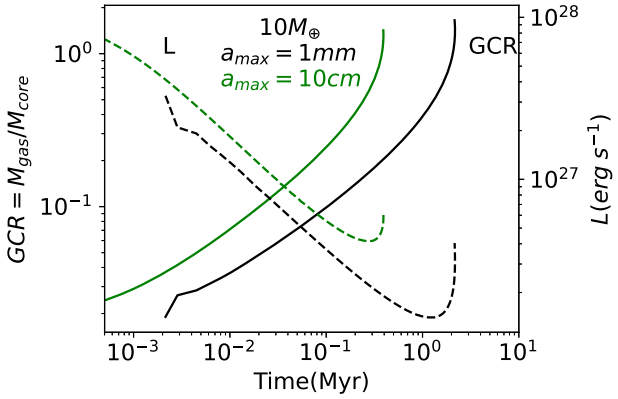

Figure 17. The gas-to-core mass ratio (solid curves) and the luminosity (dashed curves) for our Jupiter evolutionary model with the fiducial opacity (black curves) and the lower opacity (green curves).

radius. The black curves are derived with the fiducial opacity, while the green curves are derived with opacity with $a_{\rm max} = 10$ cm. We can see that our fiducial luminosity in the simulations (5.92×10^{27} ergs s^{-1}) is at the higher end of the luminosity curve, which occurs at the early contraction stage or late run-away accretion stage. The reduced luminosity in our simulations (5.92×10^{26} ergs s^{-1}) is more aligned with the typical envelope luminosity.

The resulting Jupiter envelope evolution is very similar to previous results. The 10 earth mass core can undergo runaway accretion within 10 Myr, and the reduced opacity can speed up the atmosphere accretion. These agreements are not surprising since our 3D simulations basically confirm the previous 1D analytical or semi-analytical approach. The improvement we proposed (Section 5.1) does not change the results qualitatively.

5.4 Chemical abundances of the planetary atmosphere

Although our 3D simulations produce similar planetary structure and planet evolution as previous 1D models, the 3D simulations reveal efficient mass recycling which can change the chemical abundances of the planetary atmosphere.

For a planet with a final atmosphere mass of $m_{\rm atm}$, let's assume that the initially accreted material has a fraction (f_i) of this mass in the metal. But the planet is embedded in the disc and the disc material has a fraction (f_d) of its mass in the metal. After exchanging the mass of Δm, the metal fraction of the atmosphere becomes

$$f_o = \frac{(m_{\rm atm} - \Delta m) f_i + \Delta m f_d}{m_{\rm atm}}. \quad (27)$$

If the disc has the same metallicity as the planet ($f_d = f_i$), the atmosphere's chemical abundances won't change. If all the atmosphere is recycled ($\Delta m = m_{\rm atm}$), the atmosphere metallicity will change to the disc's metallicity. Thus, both Δm and the difference between f_i and f_d are crucial for the planet's final metallicity.

From the first-order estimate, Δm cannot be higher than the local disc mass. If we assume that the planet can at most accrete the disc material within 1 disc scale height at each side of the planet, this local disc mass is 0.9, 22, 214, 1342 $M_\oplus$ if the planet is at 0.1, 1, 5, 20 au based on our adopted disc model in Section 3.1. Thus, there is a larger mass reservoir for recycling at the outer disc. On the other hand, for a radiative envelope around a 10 $M_\oplus$ core, the recycling can penetrate until $\sim$0.1 Hill radius, which corresponds to 5, 51, 253, 1012 $R_\oplus$ at these distances. For a planet at 0.1 au, almost all the atmosphere beyond the core radius ($\sim$2 $R_\oplus$) can be recycled,

while, for a planet that is far away from the star, the recycling process may only exchange a tiny fraction of the atmosphere at its surface. Overall, the planet closer to the star is more affected by disc recycling, although there is a limited amount of disc mass reservoir. Thus, discovered super-Earths or mini-Neptunes within 1 au may have local disc metallicity imprinted no matter where they formed initially in the disc.

For a planet with an outer convective envelope (e.g. due to the high luminosity from pebble accretion or runaway accretion), the recycling may penetrate to a deeper part of the atmosphere. On the other hand, these high luminosity phases can be short compared with the disc lifetime.

The other effect, $f_i - f_d$, is determined by the disc evolution and the planet migration. During planet formation, the chemical abundances of the disc change with time (e.g. Li et al. 2020) so that the initially accreted material may have a different abundance from the later surrounding disc material. At the same time, if the planet migrates in the disc, the planet can exchange with the disc material during its migration.

It is feasible to incorporate the mass exchange into the core-accretion planet formation model considering disc evolution, planet migration, and atmosphere accretion, and derive the final planet metallicity. But it is beyond the scope of this work, and we will leave it for future studies.

6 CONCLUSION

The traditional model of giant planet formation through core-accretion is derived by the 1D quasi-static approach. Recently, this 1D approach has been challenged by 3D numerical simulations which show complicated flow patterns between the envelope and the disc. Some works suggest that the significant recycling between the planetary envelope and the disc can slow or even stall the envelope accretion, potentially explaining the large number of discovered super-Earths and mini-Neptunes.

To reconcile 1D isolated envelope models and 3D disc simulations, we have carried out radiation hydrodynamic simulations for 1D and 3D isolated spherical envelopes, and 3D envelopes embedded in discs. Different from most previous 3D simulations, we heat the envelopes at specific rates so that the envelopes can achieve steady states, similar to the traditional static models. Furthermore, we have carried out the 3D isolated sphere simulations to bridge 1D models and 3D disc models. When we compare these 3D isolated sphere simulations with the 1D isolated sphere simulations, we can understand the role played by convection. When we compare them with the 3D disc simulations, we can understand the role played by disc recycling.

We have updated the opacity table for these simulations. Our new table uses the dust opacity derived from protoplanetary disc observations. The molecular and atomic opacities are also updated to cover the $\rho - T$ condition in a forming planet's envelope. Both Rosseland mean and Planck mean opacities for different metallicities have been derived and provided publicly through GitHub.

We test our 1D radiation simulations against analytical solutions. Insufficient numerical resolution can lead to artificial heating close to the inner boundary, where the density gradient is highest. Thus, a resolution study, at least with the 1D setup, is crucial for the correct envelope simulations.

When the luminosity is capable of driving convection, 3D simulations are needed since 1D radiation simulations do not allow the convective motion. With efficient energy transport by convection, the resulting envelope structure follows $\nabla \sim \nabla_{ad}$, as expected. The convective envelope in the disc has a similar structure as the isolated envelope, except with a slightly higher density due to a lower entropy.

When we increase the luminosity to make the envelope more convective, the convective motion becomes transonic which reduces the efficiency of convection. The envelope also shows significant asymmetric features since the envelope does not have time to adjust to the transonic convective motion.

When we adjust the parameters (e.g. a lower opacity, a hotter disc, or a lower luminosity) to make the envelopes radiative, we find almost identical structure among 1D or 3D isolated envelopes and 3D envelopes in discs. We provide a modified 1D semi-analytical approach which can fully reproduce our 3D disc simulations for both convective and radiative envelopes.

Using a passive scalar, we indeed observe significant mass recycling on the orbital time-scale. For the radiative envelope, recycling can only penetrate to ∼0.1–0.2 Hill radius, while, for the convective envelope, the convective motion can 'dredge up' the deeper part of the envelope so that the whole convective envelope is recycled efficiently with the disc material. This mass exchange has important implications on the proto-Jupiter's composition. For an example, a migrating proto-Jupiter can quickly (on the orbital time-scale) mix the local disc material with its envelope material so that the envelope composition does not reflect where the planet originally formed.

Although the recycling has large effects on mass exchange, it has limited effects on the envelope's thermal structure, at least for 10 $M_\oplus$ planetary cores at 5 au. We estimate various time-scales to study the effects of recycling on the envelope structure. For a convective envelope, the recycling time-scale is similar to the convective time-scale. Thus, recycling can quickly exchange the envelope material with the disc material even to the deepest part of the outermost convective envelope. For a radiative envelope, the mass recycling is only efficient beyond 0.1 r_H. Our crude estimate suggests that the cooling time-scale for the recycled material is shorter or comparable to the recycling time-scale, which may explain the limited effects of recycling on the thermal structure of the envelope.

With the updated opacity table, equation of states, and 1D models, we calculate Jupiter's atmosphere accretion with a 10 $M_\oplus$ core, and confirm that it can undergo runaway accretion within the disc's lifetime using our fiducial opacity. With a lower opacity in the envelope (opacity from 10 cm grains), the time to runaway accretion can be shorter than a Myr.

Finally, we discuss how the recycling process can affect the chemical abundances of the planet atmosphere. Both the amount of the recycled mass and the difference between the envelope metallicity and the disc metallicity are key for determining the final planet's metallicity. For a planet close to the star, the recycling process can efficiently exchange the planet's gaseous atmosphere with the disc, although there is a limited amount of disc mass reservoir at the inner disc for the exchange. Overall, the discovered super-Earths or mini-Neptunes within 1 au may have local disc metallicity imprinted no matter where these planets formed initially in the disc.

ACKNOWLEDGEMENTS

The authors thank the referee for a very helpful report, especially regarding the implications on chemical abundances of the planetary atmosphere. This research was supported by NASA TCAN award 80NSSC19K0639. All simulations are carried out using computer supported by the Texas Advanced Computing Center (TACC) at The University of Texas at Austin through XSEDE grant TG-AST130002 and from the NASA High-End Computing (HEC) program through the NASA Advanced Supercomputing (NAS) Division at Ames

Research Center. ZZ acknowledges support from the National Science Foundation under CAREER Grant Number AST-1753168. The Center for Computational Astrophysics at the Flatiron Institute is supported by the Simons Foundation. ANY acknowledges support from NASA by grant NNX17AK59G.

DATA AVAILABILITY

The data underlying this article are available in the article and in its online supplementary material.

REFERENCES

Ali-Dib M., Cumming A., Lin D. N. C., 2020, MNRAS, 494, 2440
Alibert Y., Mordasini C., Benz W., Winisdoerffer C., 2005, A&A, 434, 343
Andrews S. M. et al., 2018, ApJ, 869, L41
Armstrong G., Colgan J., Kilcrease D., Magee N., 2014, High Energy Density Phys., 10, 61
Asplund M., Grevesse N., Sauval A. J., Scott P., 2009, ARA&A, 47, 481
Ayliffe B. A., Bate M. R., 2009, MNRAS, 397, 657
Ayliffe B. A., Bate M. R., 2012, MNRAS, 427, 2597
Bate M. R., Lubow S. H., Ogilvie G. I., Miller K. A., 2003, MNRAS, 341, 213
Béthune W., Rafikov R. R., 2019, MNRAS, 488, 2365
Birnstiel T. et al., 2018, ApJ, 869, L45
Bitsch B., Johansen A., Lambrechts M., Morbidelli A., 2015, A&A, 575, A28
Bodenheimer P., Pollack J. B., 1986, Icarus, 67, 391
Brouwers M. G., Ormel C. W., 2020, A&A, 634, A15
Bryden G., Chen X., Lin D. N. C., Nelson R. P., Papaloizou J. C. B., 1999, ApJ, 514, 344
Cassisi S., Potekhin A. Y., Pietrinferni A., Catelan M., Salaris M., 2007, ApJ, 661, 1094
Castelli F., Kurucz R. L., 2003, in Piskunov N., Weiss W. W., Gray D. F., eds, IAU Symp. 210, Modelling of Stellar Atmospheres. Kluwer, Dordrecht, p. A20
Chen Y.-X., Li Y.-P., Li H., Lin D. N. C., 2020, ApJ, 896, 135
Chiang E., Laughlin G., 2013, MNRAS, 431, 3444
Cimerman N. P., Kuiper R., Ormel C. W., 2017, MNRAS, 471, 4662
Colgan J. et al., 2016, ApJ, 817, 116
D'Angelo G., Bodenheimer P., 2013, ApJ, 778, 77
D'Alessio P., Cantö J., Calvet N., Lizano S., 1998, ApJ, 500, 411
Davis S. W., Stone J. M., Jiang Y.-F., 2012, ApJS, 199, 9
Draine B. T., 2003, ARA&A, 41, 241
Ferguson J. W., Alexander D. R., Allard F., Barman T., Bodnarik J. G., Hauschildt P. H., Heffner-Wong A., Tamanai A., 2005, ApJ, 623, 585
Fontes C. J. et al., 2015, J. Phys. B: At. Mol. Phys., 48, 144014
Freedman R. S., Marley M. S., Lodders K., 2008, ApJS, 174, 504
Freedman R. S., Lustig-Yaeger J., Fortney J. J., Lupu R. E., Marley M. S., Lodders K., 2014, ApJS, 214, 25
Fuller J., 2017, MNRAS, 470, 1642
Fung J., Artymowicz P., Wu Y., 2015, ApJ, 811, 101
Fung J., Masset F., Lega E., Velasco D., 2017, AJ, 153, 124
Fung J., Zhu Z., Chiang E., 2019, ApJ, 887, 152
Gardiner T. A., Stone J. M., 2005, J. Comput. Phys., 205, 509
Gardiner T. A., Stone J. M., 2008, J. Comput. Phys., 227, 4123
González M., Audit E., Huynh P., 2007, A&A, 464, 429
Goodman J., Rafikov R. R., 2001, ApJ, 552, 793
Hakel P. et al., 2006, J. Quant. Spectrosc. Radiat. Transfer, 99, 265
Henning T., Stognienko R., 1996, A&A, 311, 291
Iglesias C. A., Rogers F. J., 1996, ApJ, 464, 943
Jiang Y.-F., 2021, ApJS, 253, 49
Jiang Y.-F., Stone J. M., Davis S. W., 2014, ApJS, 213, 7
Jones S., Andrassy R., Sandalski S., Davis A., Woodward P., Herwig F., 2017, MNRAS, 465, 2991
Kley W., 1998, A&A, 338, L37
Lambrechts M., Lega E., 2017, A&A, 606, A146
Lee E. J., 2019, ApJ, 878, 36
Lee E. J., Chiang E., 2015, ApJ, 811, 41
Lee E. J., Chiang E., Ormel C. W., 2014, ApJ, 797, 95
Levermore C. D., Pomraning G. C., 1981, ApJ, 248, 321
Li M., Huang S., Petaev M. I., Zhu Z., Steffen J. H., 2020, MNRAS, 495, 2543
Machida M. N., Kokubo E., Inutsuka S.-i., Matsumoto T., 2008, ApJ, 685, 1220
Magee N. H. et al., 2004, in Cohen J. S., Kilcrease D. P., Mazavet S., eds, AIP Conf. Ser. Vol. 730, Atomic Processes in Plasmas: 14th APS Topical Conference on Atomic Processes in Plasmas. Am. Inst. Phys., New York, p. 168
Mizuno H., 1980, Prog. Theor. Phys., 64, 544
Mizuno H., Nakazawa K., Hayashi C., 1978, Prog. Theor. Phys., 60, 699
Moldenhauer T. W., Kuiper R., Kley W., Ormel C. W., 2021, A&A, 646, L11
Movshovitz N., Bodenheimer P., Podolak M., Lissauer J. J., 2010, Icarus, 209, 616
Ormel C. W., Shi J.-M., Kuiper R., 2015, MNRAS, 447, 3512
Paardekooper S. J., Mellema G., 2008, A&A, 478, 245
Paxton B., Bildsten L., Dotter A., Herwig F., Lesaffre P., Timmes F., 2011, ApJS, 192, 3
Perri F., Cameron A. G. W., 1974, Icarus, 22, 416
Petaev M. I., 2009, Calphad, 33, 317
Piso A.-M. A., Youdin A. N., 2014, ApJ, 786, 21
Piso A.-M. A., Youdin A. N., Murray-Clay R. A., 2015, ApJ, 800, 82
Podolak M., 2003, Icarus, 165, 428
Pollack J. B., Hollenbach D., Beckwith S., Simonelli D. P., Roush T., Fong W., 1994, ApJ, 421, 615
Pollack J. B., Hubickyj O., Bodenheimer P., Lissauer J. J., Podolak M., Greenzweig Y., 1996, Icarus, 124, 62
Porter D. H., Woodward P. R., 2000, ApJS, 127, 159
Rabago I., Zhu Z., 2021, MNRAS, 502, 5325
Rafikov R. R., 2006, ApJ, 648, 666
Rosenthal M. M., Chiang E. I., Ginzburg S., Murray-Clay R. A., 2020, MNRAS, 498, 2054
Schulik M., Johansen A., Bitsch B., Lega E., 2019, A&A, 632, A118
Shakura N. I., Sunyaev R. A., 1973, A&A, 500, 33
Skinner M. A., Ostriker E. C., 2013, ApJS, 206, 21
Stevenson D. J., 1982, Planet. Space Sci., 30, 755
Stone J. M., Gardiner T. A., Teuben P., Hawley J. F., Simon J. B., 2008, ApJS, 178, 137
Stone J. M., Tomida K., White C. J., Felker K. G., 2020, ApJS, 249, 4
Szulágyi J., Mordasini C., 2017, MNRAS, 465, L64
Szulágyi J., Masset F., Lega E., Crida A., Morbidelli A., Guillot T., 2016, MNRAS, 460, 2853
Tanigawa T., Ohtsuki K., Machida M. N., 2012, ApJ, 747, 47
Wang H.-H., Bu D., Shang H., Gu P.-G., 2014, ApJ, 790, 32
Warren S. G., Brandt R. E., 2008, J. Geophys. Res.: Atmos., 113, D14
Zhang D., Davis S. W., Jiang Y.-F., Stone J. M., 2018, ApJ, 854, 110
Zhu Z., Hartmann L., Gammie C., 2009, ApJ, 694, 1045
Zhu Z., Hartmann L., Nelson R. P., Gammie C. F., 2012, ApJ, 746, 110
Zhu Z., Ju W., Stone J. M., 2016, ApJ, 832, 193
Zhu Z., Jiang Y.-F., Stone J. M., 2020, MNRAS, 495, 3494

APPENDIX A: SOURCE TERMS UNDER THE ROTATING FRAME

Since we solve the fluid equations in the rotating frame which rotates around the central star at an angular frequency of Ω_0, we need to add the Coriolis force ($-2\boldsymbol{\Omega_0} \times \boldsymbol{V}$) and the centrifugal force ($-\boldsymbol{\Omega_0} \times (\boldsymbol{\Omega_0} \times \boldsymbol{r})$) as external source terms. We want to add these two terms in a way to: 1) cancel out the central star's gravitational force and the geometrical source terms as much as possible, and 2) conserve angular momentum in the inertial frame. Since the gravitational force from the central star is the largest force in the system, any numerical imbalance between the gravitational force term and the other terms can lead to strong perturbations to a steady fluid. Besides the radial force balance, conserving the angular momentum is crucial for accurately simulating a disc in a rotating frame (Kley 1998).

Most of the derivation below is applicable to different hydrodynamical codes, although some are specifically for the Athena++ code which we will state explicitly. For the radial momentum equation, the radial Coriolis and centrifugal forces are $F_r = 2\Omega_0 v_\phi \sin\theta + \Omega_0^2 r \sin^2\theta$. For a Keplerian flow, this force needs to balance the gravitational force and the geometric source term v_ϕ^2/r. In Athena++, the gravitational force of a point mass is implemented as

$$F_* = src1i_i \frac{GM}{r_i}, \tag{A1}$$

where

$$src1i_i = \frac{1/2\left(R_{i+1/2}^2 - R_{i-1/2}^2\right)}{1/3\left(R_{i+1/2}^3 - R_{i-1/2}^3\right)}. \tag{A2}$$

Thus, we implement the radial source terms from the Coriolis and centrifugal forces using the same quantities

$$\rho F_r = \Omega_0 r_i \sin\theta_j \left(F_{\phi,k+1} + F_{\phi,k}\right) \times src1i_i + \rho\Omega_0^2 r_i^2 \sin^2\theta_j \times src1i_i\,. \tag{A3}$$

where $F_{\phi,k}$ is the Riemann flux at the constant ϕ_k interface for the density continuity equation. The first term on the right side is the Coriolis force, while the second term is the centrifugal force.

Similarly, for the θ momentum equation, the Coriolis and centrifugal forces are $F_\theta = 2\Omega_0 v_\phi \cos\theta + \Omega_0^2 r \sin\theta\cos\theta$. This force needs to balance the geometric source term ($\cot\theta\, v_\phi^2$/r) which uses the factor of $src1i_i \times src1j_j$ in Athena++ where

$$src1j_j = \frac{\sin\theta_{j+1} - \sin\theta_j}{\cos\theta_{j+1} - \cos\theta_j}. \tag{A4}$$

Thus, we implement the θ source terms using

$$\rho F_\theta = \Omega_0 r_i \sin\theta_j \left(F_{\phi,k+1} + F_{\phi,k}\right) \times src1i_i \times src1j_j + \rho\Omega_0^2 r_i^2 \sin^2\theta_j \times src1i_i \times src1j_j\,. \tag{A5}$$

In both equations (A3) and (A5), we use the Riemann flux to represent ρv_ϕ to slightly improve the accuracy.

For the ϕ momentum equation, we can absorb both the Coriolis and centrifugal terms into the divergence operator so that it is written as a conservative form (Kley 1998),

$$\frac{\partial\left(\rho\left(v_\phi + \Omega_0 r\sin\theta\right) r\sin\theta\right)}{\partial t} + \nabla\cdot\left(r\sin\theta\rho\mathbf{u}\left(v_\phi + \Omega_0 r\sin\theta\right)\right) = 0. \tag{A6}$$

If we solve equation (A6) directly using the finite volume method, we can conserve the total angular momentum $(\rho(v_\phi + \Omega_0 r_c\sin\theta_c) r_c\sin\theta_c)$ to the machine precision, where r_c and θ_c represent the distance and angle of each cell centre. Unfortunately, solving equation (A6) directly can significantly change the structure of the code. We would still like the code to solve the same set of equations no matter what coordinate systems we are using. Thus, we expand equation (A6) into the discretized form and separate the terms which are associated with the Coriolis and centrifugal forces. The time derivative of the density is replaced by the discretized continuity equation. In this way, adding the derived source term is equivalent to solving equation (A6) directly while keeping the structure of the code intact. The derived source term is

$$\begin{aligned}\rho F_\phi = & -\frac{\Omega_0\sin\theta_c\left(\cos\theta_j - \cos\theta_{j+1}\right)\Delta\phi}{r_c\Delta V}\left(r_{i+1}^4 F_{r,i+1} - r_c^2 r_{i+1}^2 F_{r,i+1} - r_i^4 F_{r,i} + r_c^2 r_i^2 F_{r,i}\right)\\ & -\frac{\Omega_0 r_c\left(r_{i+1}^2 - r_i^2\right)\Delta\phi}{2\sin\theta_c\Delta V}\left(\sin^3\theta_{j+1}F_{\theta,j+1} - \sin^3\theta_j F_{\theta,j} - \sin^2\theta_c\sin\theta_{j+1}F_{\theta,j+1} + \sin^2\theta_c\sin\theta_j F_{\theta,j}\right),\end{aligned} \tag{A7}$$

where $\Delta V = 1/3(r_{i+1}^3 - r_i^3)(\cos\theta_j - \cos\theta_{j+1})\Delta\phi$. We chose $r_c = (r_{i+1} + r_i)/2$ and $\sin\theta_c = (\sin\theta_{j+1} + \sin\theta_j)/2$, so that equation (A7) becomes

$$\begin{aligned}\rho F_\phi = & -\frac{3\Omega_0\left(\sin\theta_{j+1} + \sin\theta_j\right)\left(r_{i+1}^2 F_{r,i+1}\left(3r_{i+1} + r_i\right) + r_i^2 F_{r,i}\left(3r_i + r_{i+1}\right)\right)}{4\left(r_{i+1} + r_i\right)\left(r_{i+1}^2 + r_{i+1}r_i + r_i^2\right)}\\ & -\frac{3\Omega_0\left(r_{i+1} + r_i\right)^2\left(\sin\theta_{j+1} - \sin\theta_j\right)\left(\left(3\sin\theta_{j+1} + \sin\theta_j\right)\sin\theta_{j+1}F_{\theta,j+1} + \left(3\sin\theta_j + \sin\theta_{j+1}\right)\sin\theta_j F_{\theta,j}\right)}{8\left(\sin\theta_{j+1} + \sin\theta_j\right)\left(\cos\theta_j - \cos\theta_{j+1}\right)\left(r_{i+1}^2 + r_{i+1}r_i + r_i^2\right)}.\end{aligned} \tag{A8}$$

Since the Coriolis force does not do any work, we only add the work done by the centrifugal force in the energy equation. Again, we use the density flux (F) instead of ρv to calculate the work done by the centrifugal force.

APPENDIX B: CONSTANT RADIATION FLUX BOUNDARY CONDITION

Our 1D test problem requires us to have a constant radiation flux coming out of the inner radial boundary. Since we solve the specific intensity for the radiative transfer, we need to provide the specific intensity in all directions within the ghost zones. To maintain a constant radiation flux

at the inner boundary, the second momentum equation of the radiative transfer equation

$$\nabla \cdot \boldsymbol{P}_{r,c} = -\sigma_{T,c} \boldsymbol{F}_{r,c} \,, \tag{B1}$$

where $\boldsymbol{P}_{r,c}$ and $\boldsymbol{F}_{r,c}$ are the radiation pressure tensor and the radiation flux in the code unit, and $\sigma_{T,c}$ is the total opacity in the code unit, indicates that

$$E_{r,c}(r_g) = T_{in}^4 + 3\sigma_{T,c} \left(r_{in} - r_g\right) F_{r,c} \,, \tag{B2}$$

where r_g and r_{in} are the radial position of each ghost zone and the first active zone, and we have assumed the Eddington approximation $P_{r,c} = E_{r,c}/3$ and $E_{r,c} = T_c^4$ for the LTE condition.

Using two stream approximation, we assume that all rays pointing to the negative r direction have the same intensity I_-, while all rays pointing outwards have the intensity I_+. Then, we have

$$\begin{aligned} E_{r,c} &= I_- \times \sum_- w_- + I_+ \times \sum_+ w_+ \\ F_{r,c} &= I_- \times \sum_- w_- \mu_{r-} + I_+ \times \sum_+ w_+ \mu_{r+} \,. \end{aligned} \tag{B3}$$

where w and μ_r are the weights and r-direction cosines as defined in Davis et al. (2012), and $\sum_-$ or $\sum_+$ is the summation of all rays in negative or positive r directions. The sign of $-$ and $+$ represent rays pointing to the negative or positive r direction. If we define $\sum_- w_-$ as a_-, $\sum_+ w_+$ as a_+, $\sum_- w_- \mu_{r-}$ as b_-, and $\sum_+ w_+ \mu_{r+}$ as b_+, we can solve for I_- and I_+ as

$$\begin{aligned} I_- &= \frac{E_{r,c}/a_+ - F_{r,c}/b_+}{a_-/a_+ - b_-/b_+} \\ I_+ &= \frac{E_{r,c}/a_- - F_{r,c}/b_-}{a_+/a_- - b_+/b_-} \,. \end{aligned} \tag{B4}$$

Using $E_{r,c}$ calculated in equation (B2), we assign I_- and I_+ for rays propagating in the negative and positive r directions for every cell in the ghost zones.

This paper has been typeset from a TEX/LATEX file prepared by the author.